

# Chapter 13

## Seismic Detection of Post-perovskite Inside the Earth

Laura Cobden, Christine Thomas and Jeannot Trampert

**Abstract** Since 2004, we have known that perovskite, the most abundant mineral in the lower mantle, has the capacity to transform to a denser structure, post-perovskite, if subjected to sufficiently high temperature and pressure. But does post-perovskite exist inside the Earth? And if it does, do we have the resources to locate it seismically? In this chapter, we present an overview of what we know about the perovskite-to-post-perovskite phase transformation from mineral physics, and how this can be translated into seismic structure. In light of these constraints, we evaluate the current lines of evidence from global and regional seismology which have been used to indicate that post-perovskite is likely present in the deep mantle.

**Keywords** Post-perovskite · D'' discontinuity · Seismology · Mineral physics

### 13.1 Introduction

The radial seismic structure of the Earth's upper mantle is characterised by regions of smoothly increasing wave speeds separated by sharp discontinuities (Fig. 13.1). These discontinuities are correlated with, and almost universally accepted as resulting from, mineralogical phase transformations in  $(\text{Mg}, \text{Fe})\text{Si}_2\text{O}_4$ , of which about 60 % of the upper mantle is composed (concurrent transformations in less abundant phases enhance velocity gradients and influence the magnitude of the discontinuities). In contrast, in the lower mantle, wave speeds increase smoothly and monotonically with depth, with no major discontinuities, until about 300 km

---

L. Cobden (✉) · C. Thomas  
Institut für Geophysik, Westfälische Wilhelms-Universität, Münster, Germany  
e-mail: L.J.Cobden@uu.nl

L. Cobden · J. Trampert  
Department of Earth Sciences, Utrecht University, Utrecht, The Netherlands

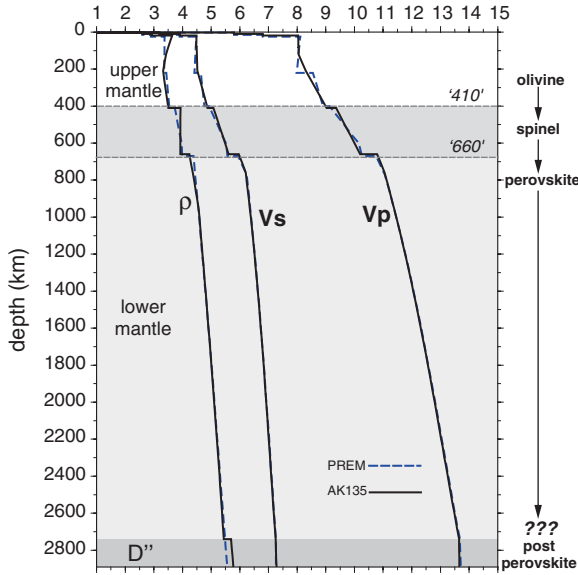


**Fig. 13.1** 1-D seismic velocity and density profiles for the Earth's mantle and associated major mineralogical phase transformations. The “410” discontinuity is associated with transformation of olivine to  $\beta$ -spinel (wadsleyite), and the “660” discontinuity is associated with transformation of  $\gamma$ -spinel (ringwoodite) to perovskite. These major transformations are accompanied by pyroxene to garnet, and garnet to perovskite, phase transitions which occur over broad depth intervals and which modify the depth and sharpness of the discontinuities at 410 and 660

above the core–mantle boundary (CMB), where a marked decrease in seismic velocity gradients is observed (Fig. 13.1). This region of anomalous seismic gradients was first noted by Gutenberg (1914) and referred to as the  $D''$  layer (Bullen 1950). While globally averaged seismic profiles show only a change in the velocity gradients at the base of the mantle, regional seismic data sets have revealed that abrupt vertical changes in wave speed do occur for both  $P$  and  $S$  waves on local to regional scales at the top of the  $D''$  region (e.g. Lay and Helmberger 1983; Baumgardt 1989; Weber 1993). These abrupt changes are usually referred to as the  $D''$  discontinuity. By 1998, more than 40 separate studies had documented observations of a  $D''$  discontinuity between  $\sim 100$  and 450 km above the CMB (see Wysession et al. 1998 for a review) in different parts of the globe, although its apparent magnitude and depth vary significantly both within and between studies.

Given the association between upper mantle seismic discontinuities and phase transformations, it is reasonable to speculate that the  $D''$  discontinuity may be related to another such transformation. Sidorin et al. (1999a, b) used geodynamic modelling to show that seismic observations of the  $D''$  discontinuity could be explained by a mineral phase transition with a Clapeyron slope of about 6 MPa/K whereby lateral variations in the depth of the discontinuity would arise from lateral variations in temperature. However, at that time, no such phase transition was known to occur. The most abundant lower mantle mineral,

(Mg, Fe)SiO<sub>3</sub> perovskite, had demonstrated great stability at high pressures (Knittle and Jeanloz 1987; Kesson et al. 1998), and while early experiments indicated that it might transform from orthorhombic to cubic or tetragonal symmetry (Wolf and Bukowinski 1987; Wang et al. 1990) or decompose into its component oxides (Meade et al. 1995; Saxena et al. 1996, 1998), such observations were later refuted and ascribed to large temperature and pressure gradients within experimental samples. Eventually, with continuing improvements in computational and experimental techniques, several research groups independently demonstrated in 2004 that MgSiO<sub>3</sub> perovskite (Pv) will transform to a higher pressure polymorph known simply as “post-perovskite” (pPv) at pressures near to or greater than the CMB (Murakami et al. 2004; Oganov and Ono 2004; Shim et al. 2004). Subsequent investigations indicated that a similar transformation occurs in FeSiO<sub>3</sub> and Al<sub>2</sub>O<sub>3</sub> perovskites (Mao et al. 2004; Oganov and Ono 2005; Caracas and Cohen 2005b). Nonetheless, large uncertainties on the precise depth of the phase transformation at high temperatures have left the question open of whether post-perovskite should exist at all within the pressure range of the Earth’s mantle.

The discovery of post-perovskite has generated much excitement within geophysics. Its dense and anisotropic crystal structure (Fig. 13.2) likely gives it distinct seismic properties relative to perovskite (e.g. Wookey et al. 2005b; Wentzcovitch et al. 2006). Post-perovskite may thus provide a convenient explanation not only for the D'' discontinuity but also much of the seismic complexity observed within the D'' layer, including large- and small-scale anisotropy (Kendall and Silver 1998; Panning and Romanowicz 2006; Wookey and Kendall 2007), internal stratification of the D'' layer (Lay et al. 2006; van der Hilst et al. 2007) and anti-correlation between long-wavelength bulk and shear wave speed anomalies (Ishii and Tromp 1999; Masters et al. 2000).

The layered structure of post-perovskite (Fig. 13.2) may also render it rheologically weak (Hunt et al. 2009; Ammann et al. 2010), and this has the potential to influence the convective evolution of the mantle. Geodynamic simulations (Nakagawa and Tackley 2011; Tackley 2012) have shown that the presence or absence of post-perovskite affects how far slabs sink in the mantle: whether they

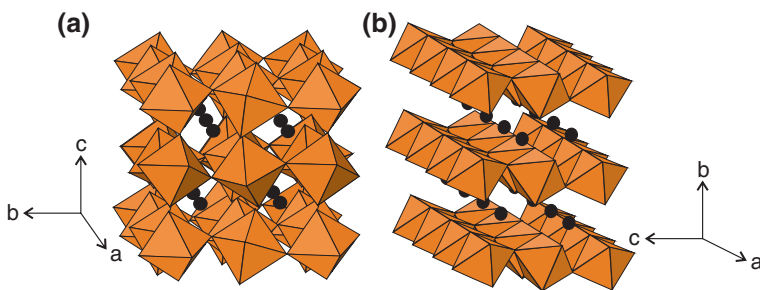


**Fig. 13.2** Crystal structures of MgSiO<sub>3</sub> perovskite (a) and post-perovskite (b). Brown octahedra represent SiO<sub>6</sub> octahedra and black spheres represent Mg cations

pile up at the core–mantle boundary or are immediately entrained upward in the global circulation. This in turn determines the chemical composition and morphology of rising plumes, which may ultimately influence the location and intensity of intraplate volcanism. As such, ascertaining whether or not post-perovskite exists inside the mantle can have a major impact on our understanding of the Earth's dynamics.

Demonstrating the existence or absence of post-perovskite in the mantle requires a careful comparison between the experimentally and theoretically derived physical properties of post-perovskite and the observed seismic properties of the deep mantle. Accordingly, we begin with a review of what constraints can be placed on the physical properties of post-perovskite and the structure of the Pv–pPv phase boundary, as determined from mineral physics observations (Sect. 13.2). We then assess whether various seismic structures in the deep Earth are compatible with, or can be used as an indicator of, the presence of post-perovskite (Sect. 13.3).

## 13.2 Mineral Physics Observations of Post-perovskite

Mineral physics constraints on the seismic and thermodynamic properties of post-perovskite come from two sources: laboratory experiments, in which rock materials are compressed and heated to the pressure and temperature conditions expected in the deep mantle, and computer simulations, which predict crystal properties using quantum mechanical theory. For the lower mantle, the experimental method of choice is the diamond anvil cell, in which a small sample of a few millimetres is compressed between two opposing anvils and heated with a laser. The structural and chemical properties of the compressed material can be determined in situ via spectroscopy or, alternatively, can be analysed post-mortem using a transmission electron microscope.

Laboratory measurements suffer from uncertainties related to (1) the physical difficulty of sustaining large yet homogeneous pressures and temperatures across small crystal samples and (2) sluggish reaction kinetics, which can prevent a sample from attaining its equilibrium structure within the time frame of the experiment. Furthermore, pressures inside the cell are determined by mixing the sample with another compound, such as gold or platinum, whose volume as a function of pressure has been previously calibrated. For a given pressure standard, at the conditions of the lowermost mantle ( $P > 100$  GPa,  $T > 2000$  K), uncertainties in the estimated pressure inside the cell due to errors in volume measurements and temperature gradients are usually cited as  $\pm 3$  to 4 GPa (e.g. Hirose et al. 2006; Hirose 2006; Ohta et al. 2008; Andraut et al. 2010) or less than  $\sim 80$  km. However, the effect of using different pressure standards can be much larger. For example, pressures inferred using a platinum reference are at least 10–15 GPa higher than those inferred from gold at  $P > 100$  GPa (Anderson et al. 1989; Akahama et al. 2002), while pressures estimated using MgO are about 5–6 GPa higher than for

gold (Hirose et al. 2008a; Grocholski et al. 2012). Some experimentalists (Fei et al. 2004; Hirose 2006) have argued that pressure calibrations based upon MgO (Speziale et al. 2001) are the most favourable choice, because the MgO scale predicts the ringwoodite-to-perovskite and perovskite-to-post-perovskite transitions at the same depths as the seismically observed 660 km and  $D''$  discontinuities, respectively. Added to this, uncertainties in temperature measurements are typically of the order of  $\pm 10\%$  at temperatures above  $\sim 2000$  K (Hirose et al. 2006; Ohta et al. 2008).

Theoretical calculations (ab initio simulations) do not suffer from the physical limitations of experiments. However, they are computationally expensive, and as a result, approximations of atomic interactions must be assumed, and many simulations are “static”, i.e. represent the material properties without thermal effects, at 0 K. Furthermore, it is particularly computationally difficult to obtain the physical properties of iron-bearing mineral assemblages (Cococcioni and de Gironcoli 2005). Consequently, computationally derived mineral properties are also associated with large uncertainties. For example, different molecular dynamic approximations, namely the local density approximation (LDA) and generalised gradient approximation (GGA), predict phase boundary pressures which differ by up to 15 GPa (e.g. Oganov and Ono 2004; Tsuchiya et al. 2004), even at 0 K.

### 13.2.1 Depth and Thickness of the Pv–pPv Phase Boundary

For a phase transition which takes place near the bottom of the mantle, where the absolute temperature is, in any case, uncertain by up to  $\sim 1500$  K (on the basis of iron melting temperatures inside the core, e.g. Oganov et al. 2002; Campbell et al. 2007; Asanuma et al. 2010; Kamada et al. 2010), the combined uncertainties in experimental measurements or ab initio calculations can translate into the difference between the transition happening above the CMB ( $\sim 135$  GPa) or below it. We have summarised in Table 13.1 the results of 29 different studies of the Pv–pPv phase boundary for a range of chemical compositions and mineralogical assemblages. A pictorial representation of those data for which the phase boundary could be determined at 2500 K, and their relation to the  $D''$  discontinuity, is shown in Fig. 13.3.

In pure  $\text{MgSiO}_3$  (the simplest possible composition), the phase boundary should be univariant, i.e. occur at a fixed temperature for a given pressure. However, the position of the phase boundary is not tightly constrained by the available data, with a significant part of the discrepancy due to the use of different pressure standards in different studies. At 2500 K, estimates of the transition pressure range from 113 GPa (c. 2450 km) to 144 GPa (i.e. well below the CMB), although most studies place the transition within the mantle (Table 13.1; Fig. 13.3). Part of the uncertainty also comes from the discrete nature of experimental data points used to construct phase equilibria. For example, the data of Murakami et al. (2004), which are among the earliest experimental observations of

**Table 13.1** Experimental and theoretical constraints on the  $P$ ,  $T$  location and thickness of the Pv–pPv phase boundary, as published up to the end of 2012

References	Technique	Pressure standard	Composition	$P$ , $T$ constraints on Pv $\rightarrow$ pPv onset	Clapeyron slope (MPa/K)	Thickness of two-phase (Pv + pPv) region (GPa)
Murakami et al. (2004)	LHDAC	Pt-1	MgSiO <sub>3</sub>	~113.5–128 GPa at 2300 K		
Shim et al. (2004)	LHDAC	Pt-2 and Ar	MgSiO <sub>3</sub>	144 ± 10 GPa at $T > 2500$ K		
Oganov and Ono (2004)	Ab initio	–	MgSiO <sub>3</sub>	~122.5 GPa at 2500 K	8.0–9.8	
Tsuchiya et al. (2004)	Ab initio	–	MgSiO <sub>3</sub>	~117–128 GPa at 2500 K	7.5 ± 0.3	
Itaka et al. (2004)	Ab initio	–	MgSiO <sub>3</sub>	98 GPa at 0 K	10	
Mao et al. (2005)	Ab initio	–	MgSiO <sub>3</sub>	113 GPa at 0 K		
Caracas and Cohen (2005a)	Ab initio	–	MgSiO <sub>3</sub>	107 GPa at 0 K		
Ono and Oganov (2005)	Ab initio and LHDAC	Pt-2	MgSiO <sub>3</sub>	~131 GPa at 2500 K	7.0	
Hirose et al. (2006)	LHDAC	Au-1	MgSiO <sub>3</sub>	113.5 GPa at 2500 K	4.7	
Hirose et al. (2006)	LHDAC	MgO	MgSiO <sub>3</sub>	120 GPa at 2500 K	11.5	
Tateno et al. (2009)	LHDAC	MgO	MgSiO <sub>3</sub>	121–123 GPa at 2500 K	13.3 ± 1	
Mao et al. (2004)	LHDAC	NaCl	(Mg <sub>0.6</sub> Fe <sub>0.4</sub> )SiO <sub>3</sub>	100 GPa at room T		
Mao et al. (2005)	Ab initio	–	(Mg <sub>0.5</sub> Fe <sub>0.5</sub> )SiO <sub>3</sub>	63 GPa at 0 K		
Caracas and Cohen (2005a)	Ab initio	–	(Mg <sub>0.5</sub> Fe <sub>0.5</sub> )SiO <sub>3</sub>	44 GPa at 0 K		
Mao et al. (2005)	Ab initio	–	FeSiO <sub>3</sub>	pPv always stable wrt Pv at 0 K		

(continued)

Table 13.1 (continued)

References	Technique	Pressure standard	Composition	$P$ , $T$ constraints on Pv $\rightarrow$ pPv onset	Clapeyron slope (MPa/K)	Thickness of two-phase (Pv + pPv) region (GPa)
Caracas and Cohen (2005a)	Ab initio	–	FeSiO <sub>3</sub>	pPv always stable wrt Pv at 0 K		
Shieh et al. (2006)	LHDAC	Pt-2, Au-2, NaCl	(Mg <sub>0.91</sub> Fe <sub>0.09</sub> )SiO <sub>3</sub>	109 $\pm$ 4 GPa at 2400 $\pm$ 400 K		
Tateno et al. (2007)	LHDAC	Au-1	(Mg <sub>0.5</sub> Fe <sub>0.5</sub> )SiO <sub>3</sub>	$\sim$ 112 GPa at 2500 K	8	>15
Tateno et al. (2007)	LHDAC	Au-1	(Mg <sub>0.25</sub> Fe <sub>0.75</sub> )SiO <sub>3</sub>	100 GPa at 2500 K		>15
Catalli et al. (2009)	LHDAC	Au-1	(Mg <sub>0.9</sub> Fe <sup>2+</sup> <sub>0.09</sub> )SiO <sub>3</sub>	$\sim$ 111 GPa at 2500 K	6.7 $\pm$ 0.5	20 $\pm$ 5
Metsue and Tsuchiya (2012)	Ab initio	–	(Mg <sub>0.9375</sub> Fe <sub>0.0625</sub> )SiO <sub>3</sub>	111 GPa at 2500 K	10	4 (at 2500 K)
Caracas and Cohen (2005a)	Ab initio	–	Al <sub>2</sub> O <sub>3</sub>	119 GPa at 0 K		
Oganov and Ono (2005)	Ab initio and LHDAC	Au-3	5 mol% Al <sub>2</sub> O <sub>3</sub> in MgSiO <sub>3</sub>	Increases pPv-in wrt MgSiO <sub>3</sub> by 5.2 GPa		
Caracas and Cohen (2005b)	Ab initio	–	5 wt% Al <sub>2</sub> O <sub>3</sub> in MgSiO <sub>3</sub>	Increases pPv-in wrt MgSiO <sub>3</sub> by 1 GPa		
Akber-Knutson et al. (2005)	Ab initio	–	6.25 mol% Al <sub>2</sub> O <sub>3</sub> in MgSiO <sub>3</sub>	127 GPa at 2500 K		>10
Tateno et al. (2005)	LHDAC	Pt-1	25 mol% Al <sub>2</sub> O <sub>3</sub> in MgSiO <sub>3</sub>	Increases pPv-in wrt MgSiO <sub>3</sub> by 7 GPa		
Zhang and Oganov (2006)	Ab initio	–	3.25 mol% Al <sub>2</sub> O <sub>3</sub> in MgSiO <sub>3</sub>	$\sim$ 142-145 GPa at 2500 K		10-30
				107.5 GPa at 0 K		
				Increases pPv-in wrt MgSiO <sub>3</sub> by 5 GPa		

(continued)

Table 13.1 (continued)

References	Technique	Pressure standard	Composition	$P$ , $T$ constraints on Pv $\rightarrow$ pPv onset	Clapeyron slope (MPa/K)	Thickness of two-phase (Pv + pPv) region (GPa)
Tsuchiya and Tsuchiya (2008)	Ab initio	–	6 mol% Al <sub>2</sub> O <sub>3</sub> in MgSiO <sub>3</sub> (“pyrolite”)	Decreases pPv-in wrt MgSiO <sub>3</sub> by 0.2 GPa per mol% Al <sub>2</sub> O <sub>3</sub>		1 (at 2500 K)
Tsuchiya and Tsuchiya (2008)	Ab initio	–	20 mol% Al <sub>2</sub> O <sub>3</sub> in MgSiO <sub>3</sub> (“MORB”)			4–5 (at 2500 K)
Nishio-Hamane et al. (2007)	LHDAC	Au-1	Mg <sub>0.85</sub> Fe <sub>0.15</sub> Al <sub>0.15</sub> Si <sub>0.85</sub> O <sub>3</sub>	~143–162 GPa at 2500 K		5–35
Catalli et al. (2009)	LHDAC	Au-1	Mg <sub>0.9</sub> Fe <sup>3+</sup> <sub>0.1</sub> Al <sub>0.1</sub> Si <sub>0.9</sub> O <sub>3</sub>	~112 GPa at 2500 K		30 ± 5
Andraut et al. (2010)	LHDAC	Au-3 and Re	Mg <sub>0.89</sub> Fe <sup>3+</sup> <sub>0.11</sub> Al <sub>0.11</sub> Si <sub>0.89</sub> O <sub>3</sub>	118–122 GPa at 3300 K	(Cf Catalli implies 7.5–12.5)	30–40
Andraut et al. (2010)	LHDAC	Au-3 and Re	(FeAl) <sub>x</sub> (MgSi) <sub>1-x</sub> O <sub>3</sub>	142 GPa at $x = 7\%$ , $T = 3300$ K $dP/dx = 0.243$ at $T = 3300$ K		
Shieh et al. (2011)	LHDAC	Pt-3 and Au-4	(Mg, Fe) <sub>3</sub> Al <sub>2</sub> Si <sub>3</sub> O <sub>12</sub>	$P \sim 124$ GPa at 2500 K assuming $C$ , slope = 7.5 Pv-out at $P > 148$ GPa, $T > 1600$ K		~30
Murakami et al. (2005)	LHDAC	Au-1	KLB-1 peridotite	~113 GPa at 2500 K		
Ono and Oganov (2005)	LHDAC	Au-3	KLB-1 peridotite	~124 GPa at 2500 K Decreases pPv-in wrt MgSiO <sub>3</sub> by 6 GPa	8.0	
Ohta et al. (2008)	LHDAC	Au-5	KLB-1 peridotite	~114–117 GPa at 2500 K	8 ± 4	3–10

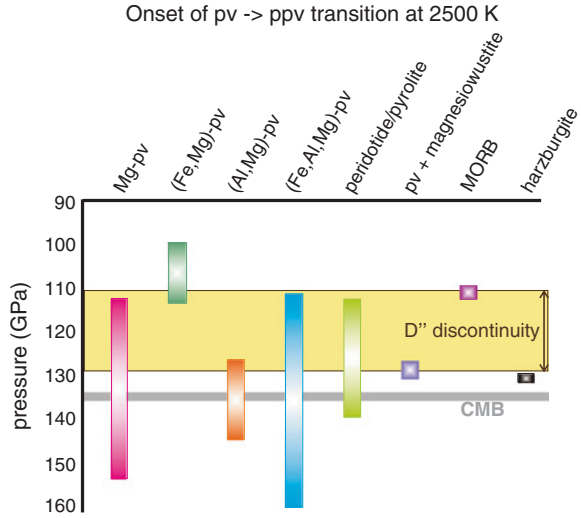
(continued)

Table 13.1 (continued)

References	Technique	Pressure standard	Composition	$P, T$ constraints on Pv $\rightarrow$ pPv onset	Clapeyron slope (MPa/K)	Thickness of two-phase (Pv + pPv) region (GPa)
Simmyo et al. (2011)	LHDAC	C	$Mg_{0.84}Fe^{3+}_{0.10}Al_{0.10}Si_{0.96}O_3$ KLB-1 peridotite	$\sim 127$ GPa at 2400 K		$\sim 3$
Simmyo et al. (2009)	LHDAC + calculations	Au-1	$(Mg_{0.91}Fe^{2+}_{0.09})SiO_3$ plus 30 % ferropericlase	$\sim 128$ GPa at 2500 K		5
Catalli et al. (2009)	LHDAC + calculations	Au-1	$(Mg_{0.91}Fe^{2+}_{0.09})SiO_3$ plus 50 % ferropericlase	$\sim 131$ GPa at 2500 K		2.2
Andrault et al. (2010)	LHDAC	Au-3 and Re	$Mg_{0.89}Fe^{3+}_{0.11}Al_{0.11}Si_{0.89}O_3$ plus ferropericlase	118 GPa at 3300 K		13
Grocholski et al. (2012)	LHDAC	Au-1	Pyrolite	140 GPa at 2500 K		30
Hirose et al. (2005)	LHDAC	Au-1	MORB	$\sim 100$ – $114$ GPa at 2500 K		
Ohta et al. (2008)	LHDAC	Au-5	MORB	$\sim 106$ – $113$ GPa at 2500 K pPv-in decreases wrt pyrolite by $\sim 4$ GPa		3–15
Grocholski et al. (2012)	LHDAC	Au-1	MORB	$\sim 107$ GPa at 2500 K		5–15
Grocholski et al. (2012)	LHDAC	Au-1	San Carlos olivine	$\sim 131$ GPa at 2500 K		$\leq 4$

LHDAC = Laser-heated diamond anvil cell. The pressure of the phase transition is given at 2500 K where possible (on the basis of experimental data points or Clapeyron slope measurements) to facilitate comparison between different studies. Pressure scales: Ar (Ross et al. 1986); Au-1 (Tsuchiya 2003); Au-2 (Shim et al. 2002); Au-3 (Jamieson et al. 1982); Au-4 (Dewaele et al. 2004); Au-5 (Hirose et al. 2008a); C (diamond) (Akahama and Kawamura 2004); MgO (Speziale et al. 2001); NaCl (Sata et al. 2002); Pt-1 (Jamieson et al. 1982); Pt-2 (Holmes et al. 1989); Pt-3 (Fei et al. 2007); Re (Zha et al. 2004)

**Fig. 13.3** Schematic diagram showing the experimentally observed onset of Pv to pPv transition at 2500 K for a range of chemical and mineralogical compositions, relative to the pressure range of the D'' discontinuity and the CMB. Each vertical bar reflects the uncertainty in pressure onset of the phase transition for a fixed composition, using the data listed in Table 13.1



pPv, constrain the boundary best at 2300 K. At this temperature, there are observations of Pv and pPv at a range of pressures, but there is a 15 GPa gap between observations of Pv and those of pPv, which puts an uncertainty of 15 GPa on the position of the phase boundary.

Adding iron and aluminium to  $\text{MgSiO}_3$  changes not only the depth of the phase boundary but creates a two-phase depth interval where both perovskite and post-perovskite coexist. A thick two-phase region is seismically relevant because even if Pv and pPv have significantly differing seismic velocities (discussed below, Sect. 13.2.3), if the transformation from one to the other is gradual, it will not generate a sharp seismic discontinuity. Further, if the depth of the phase boundary becomes too shallow, it will not be consistent with the observed depths of the D'' discontinuity, and if it becomes too deep, it will place the phase transition beyond mantle pressures. Experiments and calculations on binary systems, i.e.  $(\text{Mg}_{1-x}\text{Fe}_x)\text{SiO}_3$ , have indicated that adding  $\text{Fe}^{2+}$  to  $\text{MgSiO}_3$  will decrease the pressure of the phase boundary significantly (Mao et al. 2004, 2005; Caracas and Cohen 2005a), and measurements by different groups using different pressure standards have consistently shown that for compositions close to  $(\text{Mg}_{0.9}\text{Fe}_{0.1})\text{SiO}_3$ , the phase transformation to post-perovskite begins at around 111 GPa at 2500 K (Shieh et al. 2006; Catalli et al. 2009; Metsue and Tsuchiya 2012). Most studies show that adding aluminium has the opposite effect, increasing the phase boundary by ~5 GPa for ~5 mol%  $\text{Al}_2\text{O}_3$  (Oganov and Ono 2005; e.g. Akber-Knutson et al. 2005; Zhang and Oganov 2006), but some studies predict that it will decrease the phase boundary by ~0.2 GPa per mol%  $\text{Al}_2\text{O}_3$  (Tsuchiya and Tsuchiya 2008). Fe and Al both have the capacity to produce very thick two-phase regions: estimates of the thickness when Fe is added to the  $\text{MgSiO}_3$  range from 4–20 GPa, i.e. up to 400 km, and when Al is added, between 1 and 30 GPa, i.e. up to 600 km (Table 13.1). However, in the real Earth, we expect

both Fe and Al to be present simultaneously. Experimental observations of ternary systems,  $(\text{FeAl})_x(\text{MgSi})_{1-x}\text{O}_3$ , predict widely varying estimates of the onset of the phase transformation, from  $\sim 20$  GPa above to  $\sim 25$  GPa below, the CMB, but all studies consistently observe a broad two-phase region of about 30 GPa thickness ( $\sim 600$  km) before Pv completely disappears (Nishio-Hamane et al. 2007; Catalli et al. 2009; Andrault et al. 2010; Shieh et al. 2011).

Nonetheless, this does not imply that the Pv–pPv transition region is necessarily very broad inside the Earth, because the behaviour of the transformation is altered further when other minerals, especially (Mg, Fe)O magnesiowustite, are coexisting with the perovskite. Generally speaking, the presence of (Mg, Fe)O or the presence of Al-bearing minerals such as the “calcium ferrite (CF)-type phase”  $(\text{Na, Ca, Mg, Fe})_1(\text{Al, Si, Fe, Mg})_2\text{O}_4$  will both produce a thinner two-phase region (Catalli et al. 2009; Grocholski et al. 2012) by extracting the Fe and Al from the perovskite.

The chemical composition often taken to represent the “average” mantle is pyrolite (Ringwood 1962), although a number of studies have indicated that this may not be appropriate in the lower mantle (e.g. Cammarano et al. 2005; Cobden et al. 2009; Murakami et al. 2012). Most observations of the Pv to pPv transition in pyrolitic-type compositions (often approximated with KLB-1 peridotite, Takahashi 1986) predict a relatively narrow two-phase region with a thickness of  $\sim 3$ – $10$  GPa (Table 13.1) at pressures close to D'' depths ( $\sim 113$ – $127$  GPa at 2500 K) (Murakami et al. 2005; Ono and Oganov 2005; Ohta et al. 2006, 2008; Sinmyo et al. 2011). However, one recent study has observed that the phase transition in pyrolite may not occur until 140 GPa and may have a thickness of 30 GPa (Grocholski et al. 2012). Most of the studies of pyrolite-type compositions have used a gold pressure standard, so it is unlikely that pressure calibration effects would account for more than  $\sim 5$  GPa of the discrepancy. Grocholski et al. (2012) noted that kinetic effects (i.e. incomplete equilibration of cation distributions) can produce differences in the position of the phase boundary inferred from forward (Pv to pPv) and reverse (pPv to Pv) experiments of up to 8 GPa in multi-phase systems, so this is likely also a contributing factor. In any case, it is clear that the behaviour of the transition in pyrolitic compositions warrants further investigation. On the other hand, experimental observations of MORB, which forms a component of subducted slabs and may be present in large quantities near the base of the mantle (e.g. Tackley 2011), are much more consistent (Table 13.1): The onset of the phase transition is predicted to occur between  $\sim 100$  and 114 GPa at 2500 K, with a two-phase region between 3 and 15 GPa thick (Hirose et al. 2005; Ohta et al. 2008; Grocholski et al. 2012).

The variable behaviour of the phase boundary with respect to chemical composition and mineralogy is best understood in terms of iron and aluminium partitioning coefficients. Constraints on Fe and Al partitioning between perovskite, post-perovskite and magnesiowustite are shown in Table 13.2. Although there is a lot of discrepancy between different studies, which has been attributed to non-homogeneous cation distributions within mineral samples (Hirose et al. 2008b); complexity regarding whether Fe is present as  $\text{Fe}^{2+}$ ,  $\text{Fe}^{3+}$ , high-spin state or low-spin state; and whether or not Al is present (Andrault et al. 2010), the most recent results

**Table 13.2** Some constraints on iron and aluminium partitioning between perovskite (Pv), post-perovskite (pPv) and magnesiowustite (mw), as available up to end 2012

Reference	Composition	Partition coefficient			Value
Kobayashi et al. (2005)	(Mg, Fe)SiO <sub>3</sub> (Al-free system)	$K_{\text{Fe}^{2+}}^{(\text{mw}/\text{Pv})}$			8.3
			$K_{\text{Fe}^{2+}}^{(\text{mw}/\text{pPv})}$		3.3
				$K_{\text{Fe}^{2+}}^{(\text{Pv}/\text{pPv})}$	0.4
Murakami et al. (2005)	KLB-1 peridotite (Al-bearing system)	$K_{\text{Fe}}^{(\text{mw}/\text{Pv})}$			2.0–2.4
			$K_{\text{Fe}}^{(\text{mw}/\text{pPv})}$		7.8 ± 2.5
				$K_{\text{Fe}}^{(\text{Pv}/\text{pPv})}$	4
Ono and Oganov (2005)	Al <sub>2</sub> O <sub>3</sub> + MgSiO <sub>3</sub> (Fe-free system)			$K_{\text{Al}}^{(\text{Pv}/\text{pPv})}$	2.27
Zhang and Oganov (2006)	Al <sub>2</sub> O <sub>3</sub> + MgSiO <sub>3</sub> (Fe-free system)			$K_{\text{Al}}^{(\text{Pv}/\text{pPv})}$	2.67
Zhang and Oganov (2006)	Al <sub>2</sub> O <sub>3</sub> + MgSiO <sub>3</sub> (Fe-bearing system)			$K_{\text{Al}}^{(\text{Pv}/\text{pPv})}$	4.25
Hirose et al. (2008b)	(Mg <sub>0.91</sub> Fe <sub>0.09</sub> )SiO <sub>3</sub> Al-free system			$K_{\text{Fe}}^{(\text{Pv}/\text{pPv})}$	1.8
Andrault et al. (2010)	(Fe, Al)- bearing MgSiO <sub>3</sub> compositions			$K_{\text{Fe}}^{(\text{Pv}/\text{pPv})}$	4.2 ± 0.5
Sinmyo et al. (2011)	MgSiO <sub>3</sub> -Fe*SiO <sub>3</sub> (Al-bearing system)	$K_{\text{Fe}^{2+}}^{(\text{mw}/\text{Pv})}$			2.2
			$K_{\text{Fe}^{2+}}^{(\text{mw}/\text{pPv})}$		5.9
				$K_{\text{Fe}^{2+}}^{(\text{Pv}/\text{pPv})}$	2.68
		$K_{\text{Fe}^*}^{(\text{mw}/\text{Pv})}$			0.90
			$K_{\text{Fe}^*}^{(\text{mw}/\text{pPv})}$		4.5
				$K_{\text{Fe}^*}^{(\text{Pv}/\text{pPv})}$	5.0

$K_{\text{Fe}}^{(\text{mw}/\text{Pv})} = \frac{(X_{\text{Fe}}/X_{\text{Mg}})_{\text{mw}}}{(X_{\text{Fe}}/X_{\text{Mg}})_{\text{Pv}}}$  where  $(X_{\text{Fe}})_{\text{mw}}$  is the fraction of Fe in the (Mg, Fe)-bearing site in the mineral mw. Fe\* indicates total Fe (Fe<sup>2+</sup> plus Fe<sup>3+</sup>)

show some consistent findings: (1) Al preferentially partitions into perovskite over post-perovskite (Ono and Oganov 2005; Zhang and Oganov 2006) and (2) in the presence of Al, Fe preferentially partitions into magnesiowustite over perovskite or post-perovskite, and into perovskite over post-perovskite (Murakami et al. 2005; Hirose et al. 2008b; Andrault et al. 2010; Sinmyo et al. 2011). This means that for binary and ternary systems, both Al and Fe stabilize perovskite to higher pressures, leading to a thicker phase transition. However, in multi-phase systems, magnesiowustite will extract Fe from both the Pv and pPv and will destabilize Pv relative to pPv. This can lead to a thinner transition. Likewise, in Al-rich compositions such as MORB, where non-perovskitic Al-bearing phases (e.g. MgAl<sub>2</sub>O<sub>4</sub>) are present,

the Al will preferentially partition into these phases, destabilising Pv relative to pPv and producing a thinner transition (Grocholski et al. 2012).

In summary, the position in  $P$ - $T$  space and thickness of the phase boundary is a complex function of chemical composition, and there remains much uncertainty on its structural properties. On the basis of experimental constraints, it remains feasible that post-perovskite either does not occur at all within the pressure range of the mantle or is restricted to certain chemically distinct domains, i.e. it has a localised presence rather than a global one. Additionally, there is a strong possibility that the phase transformation occurs over a broad depth interval not compatible with a sharp seismic discontinuity. Even if the phase transition is broad, more work is required to determine the rate of conversion of Pv to pPv within the two-phase region, since this will affect its seismic visibility: If most of the phase transformation is completed within a narrow depth interval, it could once again produce a sharp seismic interface even if the overall two-phase region is broad. Current observations do indicate that rate of transformation is nonlinear with respect to depth and that the form of this non-linearity is dependent on composition (Catalli et al. 2009).

### 13.2.2 Clapeyron Slope

Many experimental observations of Pv and pPv phases are sparsely positioned in  $P$ - $T$  space and leave the gradient of the phase boundary ( $dP/dT$ ), i.e. the Clapeyron slope, completely unconstrained. In such cases, the phase boundary could be drawn with either a positive or negative slope. However, in a few experiments, observations of Pv and pPv are sufficiently proximal that the Clapeyron slope can be estimated (Table 13.1). The Clapeyron slope can also be calculated theoretically (Oganov and Ono 2004; Tsuchiya et al. 2004; e.g. Iitaka et al. 2004). While these observations unanimously indicate that the Clapeyron slope is positive (i.e. the phase transition occurs at higher temperatures as the pressure increases), estimates of its magnitude range from about 4 to 14 MPa/K. Within this variation, the Clapeyron slope seems to be composition independent (e.g. Hirose et al. 2006).

### 13.2.3 Velocity and Density Contrasts

Post-perovskite can only be detected in the Earth if its seismic properties are distinct from those of perovskite. A compilation of theoretical and experimental measurements of the changes in wave speed and density across the Pv to pPv transition is given in Table 13.3. These measurements all agree that in pure  $\text{MgSiO}_3$ , a density increase of 1–1.5 % is expected upon transformation to pPv at  $90 \text{ GPa} < P < 125 \text{ GPa}$ . Most studies also predict a significant increase in isotropic  $S$  wave velocity ( $V_S$ ) of the order of ~1–4 % and a smaller change in  $P$  wave velocity ( $V_P$ ) of less than  $\pm 1$  % (e.g. Iitaka et al. 2004; Oganov and Ono 2004;

**Table 13.3** Some calculations and in situ experimental measurements of velocity and density changes during the Pv to pPv transition; this table is not exhaustive

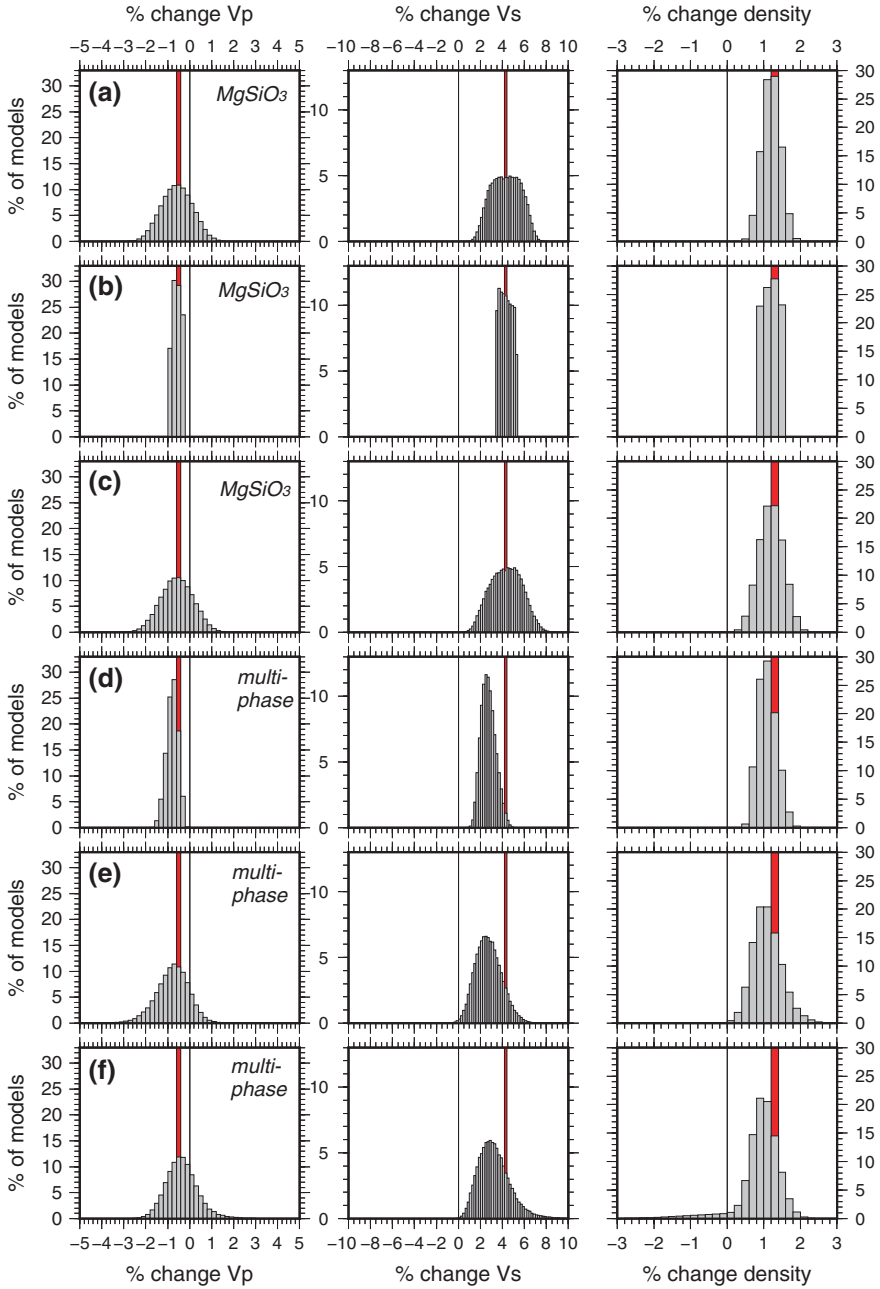
References	Technique	Composition	$P, T$	deltaVp (%, Pv to pPv)	deltaVs (%, Pv to pPv)	delta $\rho$ (%, Pv to pPv)
Murakami et al. (2004)	LHDAC	MgSiO <sub>3</sub>				+1.0 to 1.2
Tsuchiya et al. (2004)	Ab initio	MgSiO <sub>3</sub>	125 GPa, 2750 K			+1.5
Oganov and Ono (2004)	Ab initio	MgSiO <sub>3</sub>	120 GPa, 0 K	+0.3	+1.9	+1.4
Iitaka et al. (2004)	Ab initio	MgSiO <sub>3</sub>	98 GPa, 0 K	-0.1	+1	+1.4
Iitaka et al. (2004)	Ab initio	MgSiO <sub>3</sub> anisotropic	98 GPa, 0 K	+4 (VpH)	+ 3 to 7	
Wooley et al. (2005b)	Ab initio	MgSiO <sub>3</sub>	98.7 GPa, 0 K	-0.5	+ 3 to 4	+1
Caracas and Cohen (2005a)	Ab initio	MgSiO <sub>3</sub>	120 GPa, 0 K	0	+1.3	+1.5
Tsuchiya and Tsuchiya (2006)	Ab initio	MgSiO <sub>3</sub>	100 GPa, 0 K	0	0	+1.5
Tsuchiya and Tsuchiya (2006)	Ab initio	MgSiO <sub>3</sub>	120 GPa, 0 K	+0.7	+7.8	+1.5
Wentzovitch et al. (2006)	Ab initio	MgSiO <sub>3</sub>	125 GPa, 2500 K	+0.7	+2.8	
Wentzovitch et al. (2006)	Ab initio	MgSiO <sub>3</sub>	Along phase boundary of Tsuchiya et al. (2004)	0-0.5 with uncertainty up to $\pm 1$ %	+1.5 to +2.3 % with uncertainty up to $\pm 1.5$	
Murakami et al. (2007)	LHDAC	MgSiO <sub>3</sub>	125 GPa, 300 K		$\leq 0.5$	
Murakami et al. (2007)	LHDAC	MgSiO <sub>3</sub>	172 GPa, 300 K		+ 2	

(continued)

Table 13.3 (continued)

References	Technique	Composition	$P, T$	deltaVp (%, Pv to pPv)	deltaVs (%, Pv to pPv)	delta $\rho$ (%, Pv to pPv)
Ammann et al. (2010)	Ab initio	MgSiO <sub>3</sub> anisotropic	~119 GPa, ~2700 K	-0.4	+4	
Mao et al. (2005)	Ab initio	(Mg <sub>(1-x)</sub> Fe <sub>x</sub> <sup>2+</sup> )SiO <sub>3</sub>	130 GPa, 0 K			$\partial \ln \rho / \partial x \text{Fe} = 0.3$
Shieh et al. (2006)	LHDAC	(Mg <sub>0.91</sub> Fe <sub>0.09</sub> <sup>2+</sup> )SiO <sub>3</sub>	83–106 GPa, ?? K			-1.1 ± 2
Tsuchiya and Tsuchiya (2006)	Ab initio	FeSiO <sub>3</sub>	100 GPa, 0 K	-0.8	-1.7	+1.2
Caracas and Cohen (2005a)	Ab initio	Al <sub>2</sub> O <sub>3</sub>	120 GPa, 0 K	-4.3	-1.4	+1.8
Tsuchiya and Tsuchiya (2006)	Ab initio	Al <sub>2</sub> O <sub>3</sub>	120 GPa, 0 K	-0.7	-1.4	+1.8
Ono and Oganov (2005)	LHDAC	KLB-1 peridotite				~+1
Caracas and Cohen (2005a)	Ab initio	pyrolite	120 GPa, 0 K	+0.7	+2.5	+1 to 2

Note that most measurements are made at 0 or 300 K



◀ **Fig. 13.4** Histograms showing the sensitivity of  $V_p$ ,  $V_s$  and density to a phase change from perovskite to post-perovskite. Calculations assume 100 % conversion of any Pv into pPv, at 2700 km depth. **a** Pure  $\text{MgSiO}_3$  at a fixed temperature of 2600 K; the *red bars* indicate the value of  $dV_p$ ,  $dV_s$  and  $d\rho$  obtained using the elastic parameters published in Table A1 of Stixrude and Lithgow-Bertelloni (2011), while the *grey histograms* show the variation in  $dV_p$ ,  $dV_s$  and  $d\rho$  due to elastic parameter uncertainties, with elastic parameters varying at random within the uncertainty bounds published in Stixrude and Lithgow-Bertelloni (2011); **b** variation in  $dV_p$ ,  $dV_s$  and  $d\rho$  for pure  $\text{MgSiO}_3$ , with variable temperature,  $1600 < T < 2600$  K, and no elastic parameter uncertainties, *red bars* as in **a**; **c** pure  $\text{MgSiO}_3$ ,  $1600 < T < 2600$  K, with elastic parameter uncertainties; **d** multi-mineral assemblages following the compositional ranges in Cobden et al. (2012),  $1600 < T < 2600$  K, no elastic parameter uncertainties; **e** multi-mineral assemblages,  $1600 < T < 2600$  K, with elastic parameter uncertainties; **f** as in **e** but with increased iron partitioning into magnesiowustite on conversion of Pv to pPv

Caracas and Cohen 2005a; Wookey et al. 2005b; Wentzcovitch et al. 2006). One study has however indicated that post-perovskite is not necessarily much faster in  $V_S$  than perovskite at  $D''$  pressures (Murakami et al. 2007). Either way, direct comparison of observed seismic structures with these constraints is at best semi-quantitative: many mineral physics measurements are at 0 K or room temperature and do not necessarily represent what will happen at lower mantle temperatures, which may be between  $\sim 2000$  and 4000 K near the CMB (Oganov et al. 2002; Campbell et al. 2007; Cobden et al. 2009; Kamada et al. 2010; Asanuma et al. 2010). Extrapolation of seismic properties to high temperatures requires knowledge of the temperature derivatives of the elastic properties. Furthermore, the seismic wave speeds vary with chemistry, with  $\text{FeSiO}_3$  post-perovskite being  $\sim 14$  % slower in  $V_P$  and 21 % slower in  $V_S$  than  $\text{MgSiO}_3$ , and  $\text{Al}_2\text{O}_3$  post-perovskite being  $\sim 11$  % slower in both  $V_P$  and  $V_S$  (Caracas and Cohen 2005a; Tsuchiya and Tsuchiya 2006). Nonetheless, for low concentrations ( $< 5$ – $10$  mol%) of Fe and Al in post-perovskite, as is expected in a pyrolitic composition, the effect of chemistry on seismic wave speeds is predicted to be small, with the effect on the phase diagram being much more significant (Caracas and Cohen 2005a).

Since direct measurements of  $V_P$ ,  $V_S$  and density (as in Table 13.3) are only determined at a few temperatures and pressures, then inferring the seismic properties at other pressures or temperatures requires instead knowledge of the bulk and shear moduli ( $K$  and  $G$ , respectively) in addition to the density, at a fixed pressure (usually 0 GPa) and an equation of state which defines how to extrapolate these properties to lower mantle conditions. These parameters, derived from experimental and theoretical observations, typically have a non-negligible uncertainty which can affect seismic velocities significantly (e.g. Cobden et al. 2009). For realistic calculation of  $V_P$ ,  $V_S$  and density in plausible mantle compositions, one must also take into account the presence of other mineral phases, i.e. magnesiowustite, calcium perovskite  $\text{CaSiO}_3$ , free  $\text{SiO}_2$  and Al-bearing phases. It is unclear precisely how the seismic properties of individual minerals contribute to the average  $V_P$ ,  $V_S$  and density of a mixed-phase assemblage, but typically a weighted averaging scheme such as the Voigt-Reuss-Hill or Hashin-Shtrikman method is assumed. In Fig. 13.4, we show the range of possible changes in  $V_P$ ,  $V_S$  and density for pure  $\text{MgSiO}_3$  and mixed-phase assemblages in which the perovskite converts to

post-perovskite at 2700 km depth. These models were calculated using the mineral elastic parameters and uncertainty bounds on those parameters published in Stixrude and Lithgow-Bertelloni (2011), together with the equation of state of Stixrude and Lithgow-Bertelloni (2005). Uncertainties in elastic parameters alone translate into variations of ~3 %, 5 % and 1 % in  $V_P$ ,  $V_S$  and density, respectively (Fig. 13.4a). Modelling the system as a mixed-phase assemblage, i.e. including the effects of iron, aluminium, calcium, and non-silicates, rather than pure  $\text{MgSiO}_3$ , reduces the change in  $V_S$  by about 2 % (Fig. 13.3d, e) but has a much smaller effect on  $V_P$ . Increasing the partitioning of iron into magnesio-wüstite by a factor of 4 or more on converting from Pv to pPv (as predicted by experiments, Table 13.2) does not appear to produce a significant change in the seismic velocities and density (Fig. 13.4f). Thus, the range of possible velocity and density changes is dominated by uncertainties in the mineral elastic parameters, and the magnitude of the change in  $V_S$  depends strongly on chemical composition.

### 13.2.4 Anisotropy

Both *ab initio* calculations (e.g. Stackhouse et al. 2005b; Wookey et al. 2005b; Wentzcovitch et al. 2006; Ammann et al. 2010; Mao et al. 2010) and experimental observations (e.g. Murakami et al. 2004; Shieh et al. 2006; Guignot et al. 2007) of post-perovskite structure under lower mantle conditions indicate that the mineral is highly anisotropic, with a maximum compressibility, and thus minimum seismic velocity, along the *b*-axis (i.e. perpendicular to the layers of  $\text{SiO}_6$  octahedra). It is significantly more anisotropic than perovskite, and for seismic waves propagating in the crystallographic fast direction, this can enhance the velocity contrast between Pv and pPv by up to 3–7 % (Table 13.3). Calculations by Stackhouse et al. (2005a, 2006) indicate that the anisotropic structure of  $\text{MgSiO}_3$  likely does not change significantly with the addition of iron, while addition of aluminium may have a small effect.

The bulk seismic anisotropy of polycrystalline post-perovskite depends not only on the inherent anisotropy of single crystals, but also on (1) its deformation history—if the individual crystals are undeformed and randomly oriented, then the bulk anisotropy will be zero—and (2) its behaviour under deformation, in particular the crystallographic plane on which slip occurs when a deviatoric stress is applied. This has been a subject of much debate, with 4 different slip planes having been proposed for  $\text{MgSiO}_3$  pPv: (100), (010), (001) and (110) (see Nowacki et al. 2011 for a review). The main source of this variability is the experimental difficulty of working with  $\text{MgSiO}_3$  pPv, which cannot be quenched and therefore can only be observed at very high pressures (Miyagi et al. 2011). At such high pressures, only a small sample size can be used, which limits the total amount of strain that can be imparted on the sample and makes maintaining a uniform (high) temperature across the sample challenging (see Sect. 13.2.1). Depending on the magnitude and duration of the deformation, together with the grain size in an experimental sample and the mineralogy of the starting material (i.e. if pPv is synthesised directly

from Pv or from enstatite), then some experiments may observe transformation textures—texture produced during the phase transition—rather than deformation textures (Miyagi et al. 2011). To circumvent the limitations of high-pressure experiments, many studies have been done on analogue materials, primarily  $\text{CaIrO}_3$  and  $\text{MgGeO}_3$  post-perovskites, at lower temperatures and pressures that are easier to control and allow larger sample sizes. Experiments on  $\text{CaIrO}_3$  have consistently shown that slip occurs along the (010) plane in this mineral, i.e. parallel to the layering (e.g. Yamazaki et al. 2006; Miyajima et al. 2006; Walte et al. 2007; Niwa et al. 2007; Miyagi et al. 2008; Walte et al. 2009; Niwa et al. 2012). However, differences in crystal structure between  $\text{CaIrO}_3$  and  $\text{MgSiO}_3$ , namely bond lengths and bond angles, indicate that the former may not be a good analogue for deformation textures in the latter (Miyagi et al. 2008; Kubo et al. 2008; Miyagi et al. 2011).  $\text{MgGeO}_3$  appears to be more structurally similar and a better analogue (Hirose et al. 2010; Miyagi et al. 2011). The most recent experiments on  $\text{MgSiO}_3$  (at high  $P$  and low  $T$ ) and  $\text{MgGeO}_3$  (at moderate  $P$  and  $T$ ) favour slip along the (001) plane (Miyagi et al. 2010, 2011; Okada et al. 2010; Metsue and Tsuchiya 2013), which is perpendicular to the layers of  $\text{SiO}_6$  octahedra. Calculations suggest that 100 % alignment of pPv along the (001) plane would cause horizontally polarised shear waves to be 8–15 % faster than vertically polarised shear waves (Hirose et al. 2010), which is significantly higher than the 2 % difference estimated for slip along the (010) plane (Stackhouse and Brodholt 2007). Clearly, further work needs to be done to verify the slip plane and direction in pPv as this has a major influence on the magnitude of the bulk seismic anisotropy which can be induced in pPv.

Even knowing the slip plane(s) and slip vector(s) for pPv, it is still challenging to translate polycrystalline anisotropy measurements made in the laboratory into seismic observables, since the lowermost mantle is unlikely to be composed purely of (Mg, Fe) $\text{SiO}_3$ , and thus, the total seismic anisotropy in a region depends also on the anisotropic properties of any other minerals present (e.g. up to ~20 % magnesiowüstite), as well as the degree of alignment (0–100 %) of the anisotropic phases. Furthermore, measurements of seismic anisotropy in the Earth cannot easily distinguish between the alignment of inherently anisotropic crystals, i.e. lattice-preferred orientation (LPO) or any extrinsic sub-(seismic-)wavelength alignment of two materials with distinct elastic properties, i.e. shape-preferred orientation (SPO), especially at long wavelengths. Sources of SPO near the CMB could be chemical layering or aligned melt inclusions (Kendall and Silver 1998). The micro- and macro-scale seismic properties of melt, as well as the amount of melt which could be present near the CMB, are currently poorly constrained (Nowacki et al. 2011).

### 13.3 Seismic Observations

One way to test for the presence of post-perovskite is using seismic waves that sample the lower mantle. Over the years, many different waves and wave-types have been used to investigate structures near the CMB. Here, we will give an

overview of a number of these seismic probes and their ability to detect either a phase transition in or physical properties of post-perovskite. We will look at both regional and global scales.

While there are many seismic probes that are sensitive to lower mantle structure, only a few of these probes are suitable for detecting post-perovskite. These are as follows: (1) seismic discontinuities, whose depth, sharpness and impedance contrast can be compared with the Clapeyron slope, thickness and impedance change of the phase change from Pv to pPv (Sect. 13.3.1); (2) anisotropy models, whose properties can be compared with the anisotropic behaviour of pPv relative to other minerals or mineral structures (Sect. 13.3.2); and (3) tomography models of lateral variations in wave speed and density (Sect. 13.3.3). For the latter, it is essential to have models of both  $\ln V_P$  and  $\ln V_S$ , at the same spatial resolution, in order to distinguish the trade-off between temperature and composition. Additionally, including a model of the density structure  $\ln \rho$  at the same spatial resolution can provide even better constraints.

### 13.3.1 The $D''$ Discontinuity

Regional-scale seismic studies have repeatedly documented evidence for a seismic discontinuity near the base of the mantle (e.g. Lay and Helmberger 1983; Weber and Kornig 1990; Weber and Davis 1990; Davis and Weber 1990; Young and Lay 1990; Houard and Nataf 1992, 1993; Weber 1993; Weber and Wicks 1996; Weber et al. 1996; Kendall and Nangini 1996; Thomas and Weber 1997; Reasoner and Revenaugh 1999; Russell et al. 2001; Thomas et al. 2002, 2004a, b; Lay et al. 2004; Wallace and Thomas 2005; Lay et al. 2006; Avants et al. 2006; van der Hilst et al. 2007; Kito et al. 2007; Hutko et al. 2008, 2009; Chaloner et al. 2009). This discontinuity, usually referred to as “the  $D''$  discontinuity”, appears to have a complex structure, with both small and long wavelength lateral variations in its strength and depth. The discontinuity can be seen in both  $P$  and  $S$  waves (SH component), although not necessarily at the same time (e.g. Weber 1993), and in some regions, no discontinuity is observed at all (e.g. Neuberg and Wahr 1991; Chambers and Woodhouse 2006), implying that it is not necessarily a global structure. It manifests itself in seismic data as a triplicated arrival, due to refraction immediately above and/or below the discontinuity combined with reflection off the discontinuity (Fig. 13.5). The  $D''$  discontinuity probably does not appear in 1-D reference models such as PREM (Dziewonski and Anderson 1981) and AK135 (Kennett et al. 1995) because of its lateral complexity and because it is detected best at a narrow range of epicentral distances,  $\sim 60^\circ$ – $80^\circ$ , where the waves graze the discontinuity at near-critical angles and the reflection coefficient is high (Fig. 13.6). Observations of the  $D''$  discontinuity to date are thus restricted to those regions where earthquakes and seismic stations are at the correct angular separation. Regions where a  $D''$  discontinuity has been observed by one or more studies are mapped in Fig. 13.7. There are more observations for  $S$  waves than for  $P$  waves, and more observations have been gathered

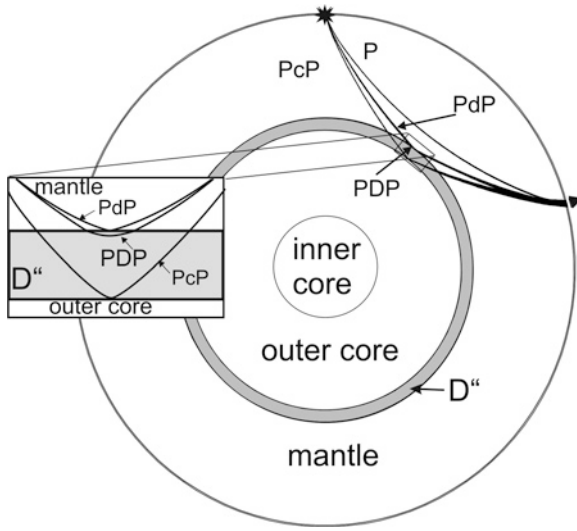


**Fig. 13.5** Schematic cross section through the Earth showing ray paths for  $D''$  phases. Earthquake indicated by *star* and seismic station indicated by *triangle*. PdP, the reflection off the top of the  $D''$  discontinuity, is sometimes known as  $P_{bc}$ , while PDP, the refraction beneath the discontinuity, is sometimes referred to as  $P_{cd}$ . Refraction immediately above the  $D''$  discontinuity may be referred to as  $P_{ab}$ . An analogous nomenclature is used for  $S$  waves

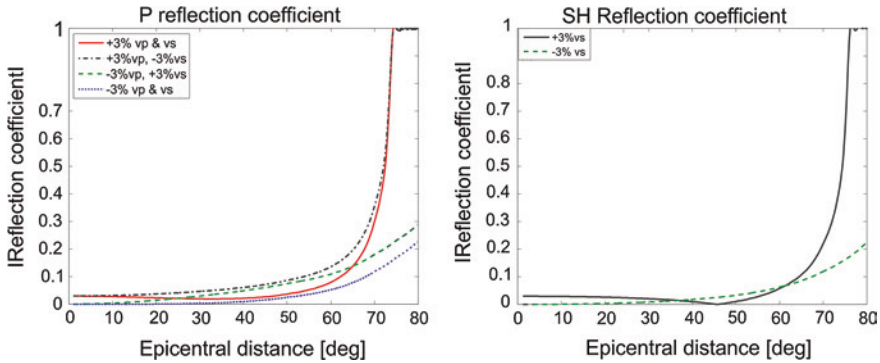


**Fig. 13.6** Reflection coefficients for  $P$  and  $S$  waves at the  $D''$  discontinuity as a function of epicentral distance

in tomographically fast regions such as the circum-Pacific than in tomographically slow regions. One possible reason for the larger amount of  $S$  wave observations is the generally larger amplitude of those waves compared with  $P$  wave triplications from the  $D''$  discontinuity.

The  $D''$  discontinuity triplication presents itself in seismic data as a weak phase which arrives later than the main  $P$  (or  $S$ ) phase but before the

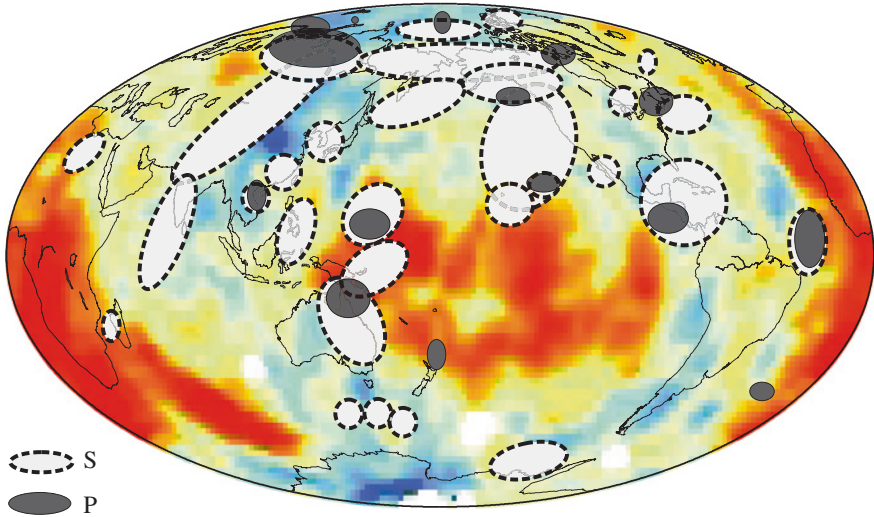


**Fig. 13.7** Locations of observations of  $D''$  discontinuity overlain on the tomography model of (Grand 2002). References for  $D''$  observations given in Sect. 13.3.1

core-reflected phase,  $PcP$  (or  $ScS$ ) (Fig. 13.5). We can be confident that the phase originates in the lowermost mantle rather than from mid-mantle or near-source scatterers (such as slabs or the Moho) if it has a slowness (move-out) intermediate between mantle refraction and core reflection (Weber 1993), and when it is seen for multiple events with different source depths (Baumgardt 1989) in the same region. This phase is given the general name  $PdP$  (or  $SdS$  for  $S$  waves) to indicate interaction with the  $D''$  discontinuity, and, depending on epicentral distance, it can be a composite of a reflection off the top of the discontinuity (known as  $P_{bc}$  or sometimes  $PdP$ ) plus a refracted wave ( $P_{cd}$  or  $PDP$ ) turning just below the discontinuity, or a reflection alone, or a refraction alone (e.g. Lay and Helmberger 1983; Weber 1993).

Even though  $PdP$  and  $SdS$  phases can sometimes be observed in single seismic traces, they are often weak signals, and various stacking techniques have been employed to enhance their visibility. These include the following: double-array stacking (Lay et al. 2004, 2006; Kito et al. 2007; Thorne et al. 2007; Lay 2008); vespagram analysis (slant-stacking) (Thomas and Weber 1997; Thomas et al. 2002; Chaloner et al. 2009); simplified seismic migration (Thomas et al. 1999; 2004b; Kito et al. 2007; Chaloner et al. 2009); Kirchhoff migration (Hutko et al. 2006); and the generalised radon transform (GRT) (Chambers and Woodhouse 2006; van der Hilst et al. 2007). Array-based methods such as vespagrams (Davies et al. 1971; Muirhead and Datt 1976) require visual inspection of individual seismograms which is time intensive, restricting studies to small data sets; on the other hand, methods such as the GRT which allow large data sets to be processed quickly are not subjected to the same level of quality control. At least part of the apparent variability

in  $D''$  structure can be ascribed to different stacking techniques, and subjective data selection between different studies (Wysession et al. 1998; Lay and Garnero 2007).

Stacking also allows assessment of the slowness of seismic phases. In single seismogram, the move-out difference between  $P$ ,  $PcP$  (or  $S$ ,  $ScS$ ) and  $PdP$  (or  $SdS$ ) is difficult to measure. Distance-dependent displays of seismic traces, or stacking techniques such as vespagrams or frequency-wavenumber analyses (for a review see Rost and Thomas 2002 or Schweitzer et al. 2002), which allow slowness estimation, can help to identify the waves, [e.g. Lay and Helmberger 1983; Weber 1993; Thomas and Weber 1997] and distinguish them from possible Moho multiples of the  $P$  wave (or  $S$  wave) or other interfering waves.

In the following subsections, we assess the suitability of seismic observations of the  $D''$  discontinuity for discriminating between the presence and absence of post-perovskite. This requires firstly an assessment of the compatibility between the structural properties of the discontinuity and those of the phase boundary, taking into account the likely biases and uncertainties in both seismic and mineralogical data sets. Secondly, where the data are of sufficient quality to allow such an assessment, a comparison against other thermo-mineralogical effects which may produce the  $D''$  discontinuity is needed. For while it is tempting to interpret the  $D''$  discontinuity in terms of a mineralogical phase change on the basis of this being the cause of the 410 and 660 discontinuities, the  $D''$  region is the boundary layer between the solid silicate mantle and the liquid outer core, where great thermo-chemical complexity is already expected in the absence of a phase transition. Thus, the  $D''$  discontinuity may instead represent reflections (or scattering, Scherbaum et al. 1997) off small- to regional-scale thermo-chemical heterogeneities, such as subducted slabs (Christensen 1989; Christensen and Hofmann 1994), piles or layers of dense and possibly primitive material (Davies and Gurnis 1986), and core–mantle reaction products (Knittle and Jeanloz 1989). The localised nature of these structures provides a plausible mechanism for the lateral variations in the depth, strength and visibility of the  $D''$  discontinuity (Sidorin et al. 1998).

### 13.3.1.1 Discontinuity Depth

By modelling the discontinuity as a sharp interface which occurs at a single depth, it is possible to constrain its depth to within  $\pm 20$  km (e.g. Weber 1993) by measuring the timing of the  $PdP$  ( $SdS$ ) arrival relative to the  $P$  ( $S$ ) or  $PcP$  ( $ScS$ ) and assuming a particular 1-D wave speed structure for the mantle. Slightly different depths may be obtained depending on whether the timing of the  $PdP$  is measured relative to the  $P$  (which gives the discontinuity's position as the depth below the Earth's surface) or relative to the  $PcP$  (which gives the position as a height above the CMB). When using the latter, care should be taken to consider the possible effects of CMB topography and the wave speed structure in between the  $D''$  discontinuity and the CMB on the travel times.

The inferred depth depends furthermore on the frequency at which the data have been filtered, which in turn is different for  $P$  and  $S$  waves, since in reality,

the discontinuity has a finite thickness to which different frequencies have variable sensitivity. *PdP* phases are usually seen at periods shorter than 10 s, while *SdS* are typically visible between ~3 and 25 s. In regions where both *PdP* and *SdS* phases are observed, the inferred depths of the discontinuity usually agree to within ~50 km. Estimates of discontinuity depth range from ~100 to 450 km above the CMB, with a global average of 250–265 km above the CMB or ~2650 km depth (Wyssession et al. 1998). Overall, it is reasonable to assume that the cited depth of a *D''* discontinuity in a particular study is accurate to within ~100 km. This variability, although large, is much smaller than the uncertainty on the depth of the Pv to pPv transition (Sect. 13.2; Table 13.1). As such, the depth of the *D''* discontinuity is compatible with the depth of the phase boundary but cannot be used to confirm the presence of post-perovskite.

### 13.3.1.2 Discontinuity Thickness

Extracting the thickness of the *D''* discontinuity is very difficult. In theory, it could be inferred from the frequency content of *PdP* or *SdS* phases (relative to the *PcP* or *ScS*) at near-vertical angles of incidence. In practice, such observations are extremely rare, due to the low reflection coefficient at pre-critical distances (Fig. 13.6), although one such study has indicated that *PdP* arrivals may be generated by a discontinuity as narrow as 8 km (Breger and Nataf in Wyssession et al. 1998). Alternatively, the thickness can be estimated by modelling the amplitude of *PdP* or *SdS* arrivals at multiple frequencies as a function of distance: a broader transition will reduce the amplitude of pre-critical arrivals relative to post-critical ones (Lay 2008). Again this is challenging because *PdP* and *SdS* arrivals can usually only be detected in a narrow distance range just before and just after critical reflection, and data from multiple events with the same reflection point at *D''* but different incidence angles are required, which are often not available. Furthermore, amplitudes are influenced by multiple factors, including 3-D discontinuity topography, and even in 1-D synthetic waveform modelling, there is a strong trade-off between the imposed width of the discontinuity and the magnitude of the velocity jump across it (see also Sect. 13.3.1.4 below). Nonetheless, these studies have indicated a maximum discontinuity thickness of ~70–90 km (e.g. Weber et al. 1996), and a recent analysis of a densely sampled region under the Cocos Plate has suggested it could be as narrow as ~30 km (Lay 2008).

The recent observation that the Pv–pPv phase transformation can, in certain multi-mineralic assemblages such as pyrolite, have a thickness of several hundred kilometres (Catalli et al. 2009; Grocholski et al. 2012) is clearly incompatible with the constraint that the *D''* discontinuity is narrower than c. 90 km. This has prompted speculation that the phase change may not be responsible for the *D''* discontinuity, or that if it is, it is only in regions with very specific chemistry such as basalt or harzburgite (Grocholski et al. 2012). However, we should bear in mind that even for a broad phase boundary, the rate of transformation is nonlinear (Catalli et al. 2009) and could be predominantly restricted to a narrow

depth interval which is compatible with observed discontinuity thicknesses. Alternatively, in the presence of shear stresses, rapid development of aligned post-perovskite grains, i.e. a sudden change in bulk anisotropy, could be responsible for a sharp seismic discontinuity in the presence of a broad phase transition (Ammann et al. 2010). At best, the <90 km thickness of the discontinuity can be used as an indication that its origin has a significant non-thermal component, since it is difficult to sustain large-amplitude temperature anomalies over length scales of a few tens of kilometres (e.g. Kaneshima and Helffrich 1999; Ricard et al. 2005). It cannot, at present, be used to detect post-perovskite.

### 13.3.1.3 Discontinuity Topography

Sidorin et al. (1999a, b) used changes in the height of the  $D''$  discontinuity in combination with long-wavelength tomographic models to deduce that if tomographic wave speed variations represented lateral variations in temperature, then the discontinuity could correspond to a phase transformation with a Clapeyron slope of +6 MPa/K. This falls within the range of Clapeyron slopes seen experimentally and theoretically for the Pv to pPv phase boundary (Table 13.1; Sect. 13.2.2), and subsequently, variations in discontinuity depth have been used to estimate temperature variations near the CMB (Lay et al. 2006; van der Hilst et al. 2007). However, given that the depth of the Pv–pPv transition can vary strongly as a function of chemistry and mineralogy, and that its visibility may also be influenced by anisotropy, it is potentially hazardous to interpret  $D''$  topography purely in terms thermal effects on the Pv–pPv phase boundary. At the time of the modelling of Sidorin et al. (1999a, b), there were limited observations of the  $D''$  discontinuity in the central Pacific; subsequently, studies have found that the discontinuity in this region is too shallow to be compatible with Sidorin et al.'s models, and this may be indicative of chemical effects on the phase boundary (e.g. Lay and Garnero 2007; Ohta et al. 2008). Furthermore, Hutko et al. (2006) have mapped 100-km amplitude undulations in the depth of  $D''$  reflections over lateral distances of 200–300 km, which would require temperature variations of 500–1000 K that are geodynamically difficult to explain.

A refinement of the method of Sidorin et al. (1999a, b) was performed by Sun et al. (2006, 2007) and Sun and Helmberger (2008) using updated tomography models and allowing for simple changes in chemistry. They found that observations of  $D''$  topography could be explained by a phase boundary with a Clapeyron slope of ~9 MPa/K, if the magnitude of the velocity jump across the discontinuity is laterally variable and if short-wavelength undulations are attributed to scattering off a buckled slab. While it is clearly possible to model  $D''$  discontinuity topography in terms of Clapeyron slopes plus compositional heterogeneity, such modelling is not uniquely diagnostic of the presence of post-perovskite because it does not rule out the possibility that alternative structures can fit the data.

### 13.3.1.4 Velocity and Density Contrasts

The impedance contrast across the  $D''$  discontinuity may be our most diagnostic tool for assessing if the discontinuity is generated by post-perovskite. In principle, the polarity of  $PdP$  and  $SdS$  waveforms indicates whether the impedance change is positive or negative, and the amplitude gives an indication of the magnitude of the change. At pre-critical distances, the waveforms are sensitive to both density and velocity, while at critical and post-critical distances where the waves graze the discontinuity obliquely (and where most observations are obtained), the waveforms are primarily sensitive to velocity changes (Lay and Garnero 2007). There are two main difficulties in measuring impedance contrasts. The first is that from a modelling perspective, there is always a trade-off between the imposed thickness of the discontinuity and magnitude of the velocity change across it. At best, it is possible to give a range of discontinuity thicknesses and velocity jumps compatible with a given seismic observation of  $PdP$  or  $SdS$ . The second—and major—issue is that 3-D topography on the discontinuity can lead to focussing and de-focussing of  $PdP$  and  $SdS$  waveforms, which may alter their amplitude significantly. To date, most estimates of velocity jumps at  $D''$  have been based upon full-waveform reflectivity modelling in 1-D (e.g. Weber 1993; Kito et al. 2007; Chaloner et al. 2009) or ray tracing in 2-D (Thomas and Weber 1997), which cannot accurately incorporate the effect of 3-D topography. Full-waveform modelling of the  $D''$  discontinuity in 3-D at the high frequencies at which it is observed is currently beyond available computational capacity. However, a few studies in 2.5-D have been or are being performed (e.g. Thorne et al. 2007); (Hempel et al., article in preparation). Investigations by Hempel et al. (pers. comm.) indicate that if the  $D''$  discontinuity is dipping more steeply than  $\sim 40^\circ$ , then it becomes seismically invisible along the great circle path, i.e. the direction in which data are stacked for vespigram analysis, and if it dips at shallower angles, then the amplitudes of the  $D''$  reflection may still be strongly influenced.

Further uncertainties arise from stacking procedures, which assume that either multiple events or multiple receivers are sampling the same reflection point at  $D''$ , when in practice, they are sampling the structure, perhaps non-uniformly, within a range of several degrees, so that the image obtained is a smeared average of any 3-D variations in topography and velocity structure of the discontinuity within that region. Added to this, for a given propagating wave, the 1-D Fresnel zone at  $D''$  depths is about  $3.5^\circ \times 7^\circ$  ( $\sim 230 \times 460$  km) for  $S$  waves with periods of around 6 s and  $2^\circ \times 4^\circ$  ( $\sim 130 \times 260$  km) for  $P$  waves with periods of around 1 s (Weber 1993), meaning that  $P$  and  $S$  waves for a given event are not sampling exactly the same structure and the resolution of topography within those ranges is questionable.

In general, 1-D reflectivity modelling indicates that velocity contrasts smaller than about 1 % are unlikely to be detected (e.g. Weber 1993). Thus, absence of a visible  $PdP$  or  $SdS$  arrival does not equate to the absence of a  $D''$  discontinuity; it may well mean that the impedance contrast is too small to be seen above the noise or that the topography de-focusses the signal. Gaherty and Lay (1992)

and Flores and Lay (2005) also noted that due to the distance-dependent properties of the reflection coefficient, it is easier to detect velocity increases than velocity decreases, leading to an observational bias towards detecting velocity increases in acquired data sets. We further note that the reflection coefficient is dependent on both the  $P$  and  $S$  velocity jump, and in the case of a positive  $S$  wave contrast and negative  $P$  wave contrast, the reflection coefficient of  $PdP$  is larger than if  $P$  and  $S$  wave speeds both increase or both decrease (Fig. 13.6). For these reasons, interpretation of discontinuity structure in terms of its apparent geographic distribution (Fig. 13.7) is not advised. For example, if the  $D''$  discontinuity were to be observed globally, it would be likely to be caused by one single effect, with a phase change in perovskite being the most plausible option. The fact that it has only been observed in regional-scale studies leaves the possibility open that it could still be global, but seismically invisible in some regions, or that it is regional and caused by multiple different regional structures including subducted material. In addition to the bias introduced by wave-propagation complexity, the apparent observability of the  $D''$  discontinuity also depends heavily on the limited distributions of earthquakes and seismic arrays.

Waveform polarities are a more robust seismic observable than waveform amplitudes because they do not change with epicentral distance (Fig. 13.8), and to our knowledge, they are not modified by the discontinuity thickness or velocity gradients. However, polarity measurements are most reliable when the data show a clear core-reflection phase ( $PcP$  or  $ScS$ ) and when it has been verified that the polarities are not modified by the earthquake radiation pattern, i.e. that  $P$ ,  $PdP$  and  $PcP$  all travel within the same quadrant of the focal mechanism. In such cases, reflectivity modelling (e.g. Weber 1993; Kito et al. 2007; Chaloner et al. 2009) demonstrates that the polarity of the  $PdP$  waveform will be the same as that of the  $P$  and  $PcP$  (“positive polarity”) for a velocity increase at the  $D''$  discontinuity, whereas the polarity of the  $PdP$  will be reversed relative to  $P$  and  $PcP$  for a velocity decrease (“reverse polarity”; likewise for  $S$  wave phases)—Fig. 13.8. An example of a vespa-gram (slant stack) for a South American earthquake which samples  $D''$  beneath the Caribbean is shown in Fig. 13.9. In this example, the polarity of the  $PdP$  indicates a negative  $P$  velocity jump at  $D''$  and the polarity of the  $SdS$  indicates a positive  $S$  velocity jump. It can be shown (Cobden and Thomas 2013) that even in the absence of amplitude measurements, polarities can discriminate between different thermo-chemical origins for the  $D''$  discontinuity, assuming that velocity contrasts greater than 1 % are needed to see a  $PdP$  or  $SdS$  phase (Fig. 13.9).

Despite the numerous pitfalls in estimating velocity changes, in some regions, consistent waveform polarities and amplitudes have been observed for multiple events. In these regions, it is perhaps reasonable (as a first-order approximation) to attempt to interpret the waveforms in terms of plausible thermo-chemical structures. Initially, such studies have been simple compatibility tests noting an agreement between the  $S$  and  $P$  velocity changes expected for conversion of  $MgSiO_3$  Pv to  $pPv$  (Table 13.3) and the estimated velocity changes across the  $D''$  discontinuity (Wookey et al. 2005b). The agreement is especially good in the Caribbean, i.e. beneath the Cocos Plate, where large increases in  $S$  wave speed (1–3 %) are

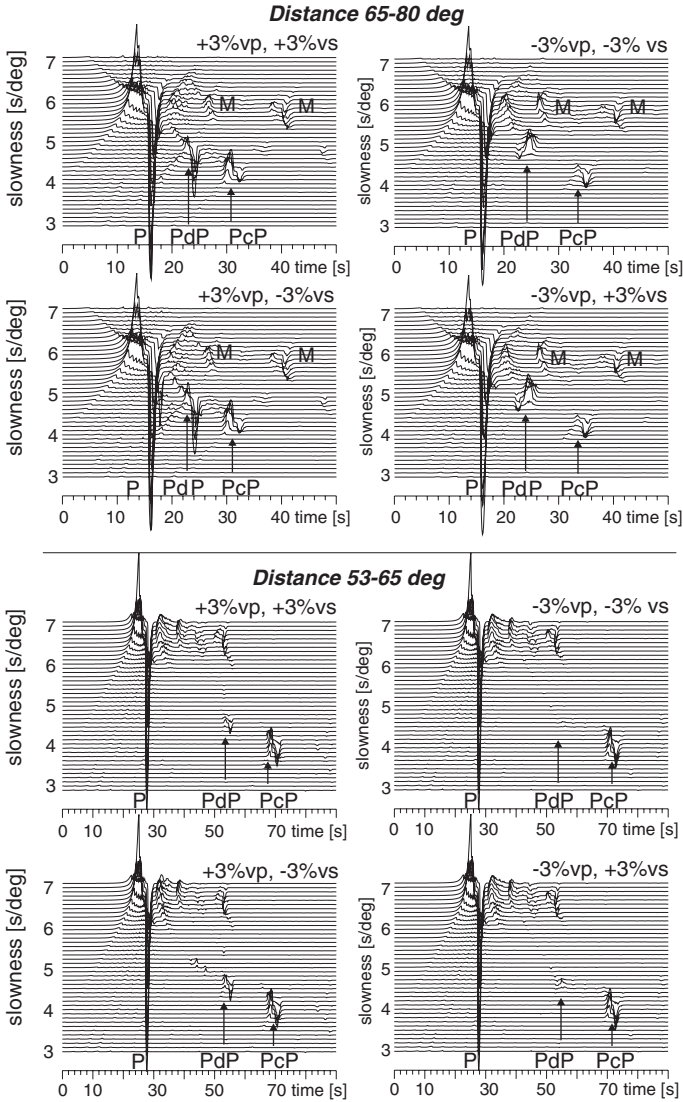
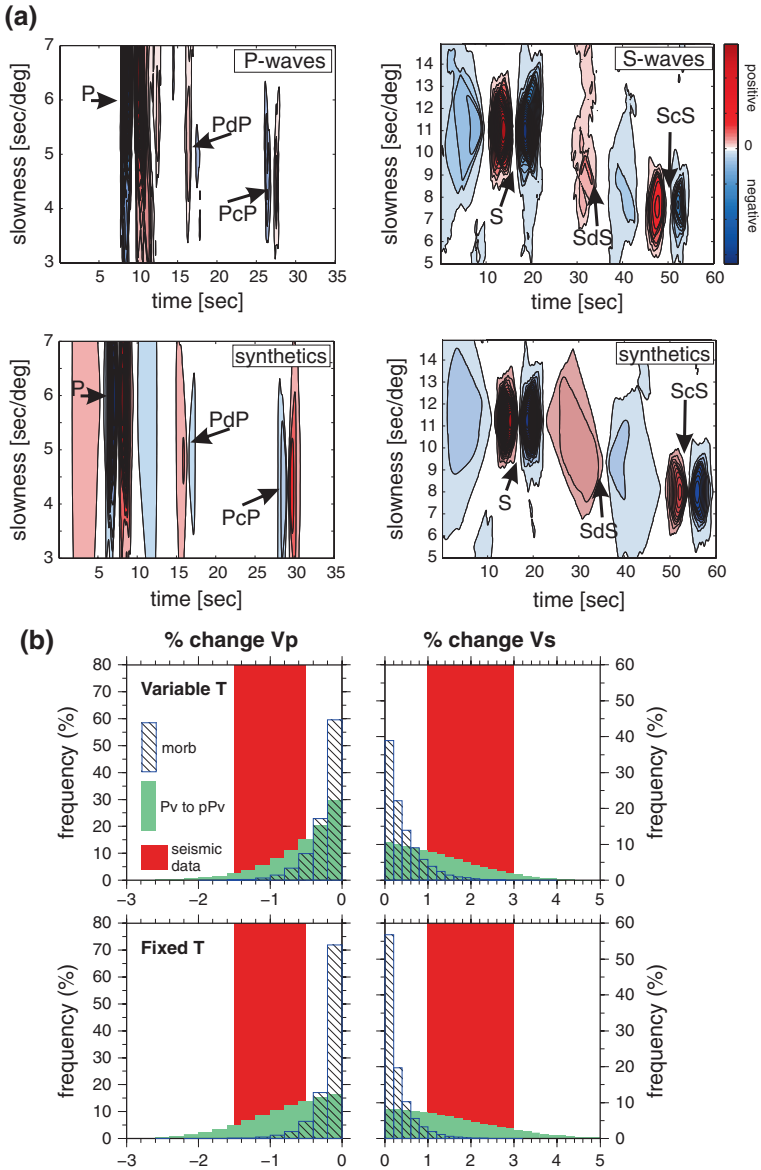


**Fig. 13.8** *PdP* waveform polarity and amplitude as a function of epicentral distance, and for *P* and *S* wave speed increases and decreases. For a 1-D earth model, the polarity does not change with epicentral distance. Note the enhanced visibility of the *PdP* phase when the change in  $V_p$  is the opposite sign to the change in  $V_s$ , and the reversal of the *PdP* polarity for *P* wave speed decreases compared to *P* wave speed increases

seen in conjunction with negative (up to  $-3\%$ ) or small positive ( $<1\%$ ) changes in  $P$  wave speed (e.g. Lay and Helmberger 1983; Kendall and Nangini 1996; Ding and Helmberger 1997; Lay et al. 2004; Thomas et al. 2004a; Kito et al. 2007; Hutko et al. 2008). The example given in Fig. 13.9 shows synthetic vespagrams for a  $P$  velocity decrease of  $1\%$  and  $S$  velocity increase of  $2\%$  that are compatible with the waveform amplitudes and polarities of the real data.

It is more problematic to invoke post-perovskite for explaining observations of the  $D''$  discontinuity underneath Siberia/Eurasia, where large-amplitude, positive polarity  $PdP$  phases, indicative of large ( $1-3\%$ ) increases in  $P$  wave speed, have been documented by multiple studies (e.g. Weber and Davis 1990; Houard and Nataf 1992; Weber 1993; Scherbaum et al. 1997; Thomas and Weber 1997). Thomas et al. (2011) suggested that these large  $P$  wave speed increases may still be reconciled with a phase change from  $Pv$  to  $pPv$ , if the  $pPv$  grains are aligned due to flow, and the seismic waves preferentially sample the fast crystallographic direction. This hypothesis was based upon observations of opposite-polarity  $PdP$  waveforms for three source–receiver combinations with ray paths intersecting at  $45^\circ$  beneath Eurasia, compared with theoretically predicted velocity jumps due to anisotropic  $pPv$  underlying isotropic  $Pv$ . In this study, one source–receiver combination had a different geographic reflection point, so the varying polarities could also have arisen from different physical structures at the reflection points rather than anisotropy. To test this possibility, Cobden and Thomas (2013) attempted to model the polarities and amplitudes with a range of isotropic mineral structures, with and without post-perovskite. Using the mineral physics parameters compiled by Stixrude and Lithgow-Bertelloni (2011) and a Monte Carlo thermodynamic modelling procedure, they found that it is statistically difficult to generate large  $P$  velocity increases at the same time as large  $S$  velocity increases via phase change from  $Pv$  to isotropic  $pPv$  in multi-mineralic assemblages, whereas it is relatively straightforward to generate such velocity jumps using subducted oceanic crust. On the other hand, in the Caribbean, the waveform polarities and amplitudes are best fit by a phase change from  $Pv$  to isotropic  $pPv$ . For example, in the event shown in Fig. 13.9, from a sample of 1 million synthetic thermo-chemical models, the proportion of models generating a  $V_P$  decrease of  $1 \pm 0.5\%$  and  $V_S$  increase of  $2 \pm 1\%$  via conversion of  $Pv$  to  $pPv$  within a multi-mineralic assemblage is  $21\%$ , whereas the percentage of models which generate these velocity changes via reflection off basaltic material is  $0.04\%$ . The percentage of models which fit only the polarities (i.e. positive  $SdS$  and negative  $PdP$  regardless of the amplitude) via conversion of  $Pv$  to  $pPv$  is  $91\%$ , compared with  $4\%$  via reflections off basaltic material.

Overall, we can surmise that post-perovskite can fit the apparent velocity jumps at the  $D''$  discontinuity (a) globally, if anisotropy is involved, or (b) only in specific locations, if isotropic. The latter scenario requires that the  $D''$  discontinuity would be generated by different structures in different regions, perhaps not entirely unreasonable given the thermo-chemical complexity of the CMB region, although Occam's razor would favour the first scenario. In some regions (e.g. the Caribbean), post-perovskite appears to be the easiest way to fit the velocity



◀ **Fig. 13.9** **a** Waveform polarity and amplitude observations for the Caribbean, displayed as 4th-root vespagrams (Davies et al. 1971). *Top row* shows real data; the *PdP* waveform has the opposite polarity to the *P* and *PcP* waveforms, indicating a velocity decrease at  $D''$  (see Fig. 13.8), while the *SdS* has the same polarity as the *S* and *ScS*, indicating a velocity increase at  $D''$ . The amplitude of the *PdP* relative to *P* and *PcP*, and the *SdS* relative to *S* and *ScS*, can be reproduced synthetically (*second row*) by assuming a  $-1\%$  velocity change in  $V_p$  and a  $+2\%$  change in  $V_s$  at 2605 km depth. **b**  $\Delta V_p$  and  $\Delta V_s$  distributions for those thermo-chemical models from an initial set of 1 million in which both an increase in  $V_s$  and a decrease in  $V_p$  (consistent with the waveform polarities in **a**) are seen. *Green* transformation of  $Pv$  to  $pPv$  in a multi-mineralic assemblage; *black stripes* = change in MORB content across  $D''$ ; *red bars* velocity changes consistent with the waveform amplitudes shown in **a**. While a large number of models in which there is a phase change from  $Pv$  to  $pPv$  can fit the waveform amplitudes, it is difficult to generate simultaneously large ( $>1\%$ ) increases in  $V_s$  and large ( $>1\%$ ) decreases in  $V_p$  via a change in MORB content at  $D''$ . *Upper row* results when the temperature is allowed to change across the  $D''$  discontinuity. *Lower row* results when temperature is kept fixed across the discontinuity

changes compared to alternative thermo-chemical structures. However, given the complexity of inverting for waveform amplitudes, we should remain open to other possibilities, including the effects of 3-D scattering off folded/buckled slabs (e.g. Hutko et al. 2006) (i.e. short-wavelength topography). While the  $D''$  discontinuity is seismically compatible with post-perovskite, it does not yet provide incontrovertible evidence for it.

### 13.3.1.5 Double Discontinuities

In the presence of a thermal boundary layer at the base of the mantle (Lay and Garnero 2004), in which the temperature increases rapidly, it has been suggested that a back transition of  $pPv$  to  $Pv$  may occur near the CMB (Hernlund et al. 2005), due to the positive Clapeyron slope of the phase boundary in the presence of high temperatures. If this happens, two seismic discontinuities could be generated, the upper one corresponding to the forward transformation of  $Pv$  to  $pPv$  and the lower one corresponding to the back transformation. Several studies have presented seismic evidence for such a double discontinuity beneath the Pacific and the Caribbean (Thomas et al. 2004a; Avants et al. 2006; Lay et al. 2006; Kito et al. 2007; van der Hilst et al. 2007; Hutko et al. 2008), although it is not always clear if the secondary waveform represents an out-of-plane arrival from a dipping reflector (Flores and Lay 2005; Hutko et al. 2006) or side lobes on the first arrival. Flores and Lay (2005) indicated that it is more difficult to detect a velocity decrease than an increase, and for the post-perovskite transition, a decrease in  $S$  wave velocity is expected for the back transformation. This means that even if double discontinuities exist, the lower reflector may not be detected. However, geodynamic modelling by Hernlund et al. (2005) predicts that the velocity contrast of the lower reflector should be much larger than that of the upper one, and theoretically, these large negative changes may be detected (e.g. Fig. 13.6). With careful analysis of waveform polarities and amplitudes, together with improved

understanding of and ability to map discontinuity topography, interpretation of double discontinuities may be a fruitful area of future research. However, one should bear in mind, as for the upper discontinuity, a deeper discontinuity can have multiple causes, including ULVZs (Lay and Garnero 2007) or slabs (Thomas et al. 2004b), or thermal effects (Kawai and Tsuchiya 2009), and attributing it to post-perovskite is only appropriate with the exclusion of other explanations. If the lower discontinuity is indeed due to a back transformation of pPv to Pv, the depth between the two discontinuities should be anti-correlated (e.g. Hernlund et al. 2005), assuming they are not modified by chemical heterogeneity. Unfortunately, there are too few places yet to study this anti-correlation, but one indication of such anti-correlation can be seen in van der Hilst et al. (2007).

### 13.3.2 Anisotropy

The anisotropic structure of the Earth's lower mantle as derived from seismic observations has been discussed extensively in a number of excellent reviews (e.g. Kendall and Silver 1998; Wookey and Kendall 2007; Nowacki et al. 2011), and so we shall only summarise the features which may be pertinent to the detection of post-perovskite. Although post-perovskite is anisotropic for both  $P$  and  $S$  waves, the vast majority of mantle anisotropy studies are based upon  $S$  waves. This is because with  $S$  waves, there is the possibility to measure shear wave splitting, which is the difference in travel time between horizontally polarised (SH) and vertically polarised (SV) waves propagating in the same direction, and can be readily deduced from the radial and transverse components of a seismogram. Splitting occurs whenever a (polarised) transverse wave encounters an anisotropic medium; since  $P$  waves vibrate longitudinally, then they do not become split on encountering anisotropic media. Thus,  $P$  wave anisotropy can only be measured by multi-azimuthal sampling of the same target region, for which data are much sparser due to limited source–receiver configurations.

In global studies, seismic anisotropy in the Earth may be broadly divided into two categories: vertically transverse isotropy (VTI), which describes the difference in wave speed between radially (i.e. perpendicular to the CMB) and tangentially (CMB-parallel) propagating waves, and azimuthal anisotropy, which describes the difference in horizontal wave speed as a function of azimuth at a given depth. Many regional studies describe anisotropic structure in terms of tilted transverse isotropy (TTI) which, like VTI, assumes that the anisotropy is hexagonally symmetric, but while VTI assumes a vertical axis of symmetry, in TTI, the axis is (as the name suggests) inclined from the vertical. In theory, TTI could be decomposed into a VTI and azimuthal components although in practice, this is not the conventional parameterisation.

Global inversions for a 1-D anisotropy model assume that the anisotropy in the Earth is purely VTI. The degree of anisotropy at a given depth may then be expressed by the parameter  $\xi = V_{\text{SH}}^2/V_{\text{SV}}^2$ . Two studies using normal modes and/

or body waves have shown that while  $\xi \approx 1$  throughout most of the lower mantle, i.e. on average the lower mantle is nearly isotropic, in the  $D''$  region,  $\xi$  becomes greater than 1 (Montagner and Kennett 1996; Panning and Romanowicz 2006). Since post-perovskite is more anisotropic than perovskite, then qualitatively this observation is compatible with the hypothesis that the  $D''$  discontinuity is associated with a phase transformation from Pv to pPv and that there is a significant amount of deformed pPv in the  $D''$  region. Panning and Romanowicz (2006) suggested that such deformation could be generated by a general transition from vertical to horizontal flow associated with the mechanical boundary layer of the CMB (e.g. as sinking slabs fold at the CMB). However, a third study by Kustowski et al. (2008) found that while the average  $V_{SH}$  is greater than  $V_{SV}$  within  $D''$ , the difference is a factor of 5 smaller than that given by Panning and Romanowicz and that the inferred magnitude trades off strongly with  $P$  wave velocity in the outer core, which may not be tightly constrained. In a further study using a Monte Carlo model space search, Beghein et al. (2006) found no significant departure of  $\xi$  from PREM. However, the normal mode data did seem to require a 1-D (VTI)  $P$  wave anisotropy, although Beghein et al. (2006) noted that it trades off with density. Therefore, it is currently uncertain how robust the observation of  $\xi > 1$  is.

Both global and regional seismic studies have attempted to map lateral variations in VTI at  $D''$  depths. Although different studies do not always agree (especially in the central Pacific), and sometimes, it is not appropriate to assume the radial symmetry of VTI, a fairly robust feature is the observation that  $V_{SH} > V_{SV}$  (typically by 1–3 %) in parts of the circum-Pacific (e.g. Lay and Young 1991; Matzel et al. 1996; Garnero and Lay 1997; Fouch et al. 2001; Panning and Romanowicz 2004, 2006; Usui et al. 2005; Thomas et al. 2007). These circum-Pacific regions are associated with subducted slabs. On the basis of this, Miyagi et al. (2010) applied their experimental observations of slip on the (001) plane in pPv to a geodynamic model of the lower mantle (McNamara and Zhong 2005) in order to compute the textural development in subducting slabs as they enter  $D''$ . They found that within the slabs, the (001) planes became aligned sub-parallel to the CMB, leading to the generation of  $V_{SH} > V_{SV}$  anisotropy compatible with seismic observations. Similar calculations by Merkel et al. (2007) which assumed instead slip on the (010) plane could not reproduce the seismic observations. However, if it is true that slip does occur on the (001) plane, then this result is another seismic feature of the  $D''$  region which is compatible with the presence of post-perovskite.

At present, observations of azimuthal anisotropy or TTI (e.g. Maupin et al. 2005; Wookey et al. 2005a; Rokosky et al. 2006; Thomas et al. 2007; Wookey and Kendall 2008; Long 2009; Nowacki et al. 2010) are not, per se, uniquely diagnostic of post-perovskite, because it is not clear how to distinguish LPO anisotropy in pPv from LPO anisotropy in other minerals (i.e. magnesiowüstite) or from SPO (Kendall and Silver 1998; Nowacki et al. 2011). However, we foresee that the most immediately applicable use of azimuthal anisotropy (in relation to post-perovskite) would be for studies of waveform polarities and amplitudes at the  $D''$  discontinuity, as implemented by Thomas et al. (2011) (and as discussed in

Sect. 13.3.1.4). In order to measure anisotropy across the  $D''$  discontinuity accurately, multi-azimuthal coverage of the same region by multiple raypaths—to determine  $PdP$  and  $SdS$  waveforms as a function of azimuth—would be required (Wookey and Kendall 2008; Nowacki et al. 2010; Thomas et al. 2011). Multi-azimuthal sampling would also help to constrain the 3-D morphology of topography on the discontinuity. Currently, such studies are unfortunately hindered by the limited distribution of seismic arrays (and earthquakes). Even if the presence and orientation of azimuthal anisotropy would be accurately constrained, in order to demonstrate that it is the result of post-perovskite, the anisotropic velocities of multi-mineralic assemblages and not only pure  $MgSiO_3$  should be computed, together with calculations involving anisotropy in magnesiowustite rather than post-perovskite. Furthermore, much more work remains to be done on understanding the deformation mechanisms within  $D''$ , in addition to the seismic properties of melt inclusions which may generate SPO.

### 13.3.3 Long-Wavelength Seismic Structures

#### 13.3.3.1 Presence or Absence of Post-perovskite at a Global Scale

Long-wavelength seismic tomography may also provide clues about the existence of post-perovskite in the Earth (e.g. Houser 2007; Cobden et al. 2012; Mosca et al. 2012). Since post-perovskite is most likely to occur near the CMB (Table 13.1), it is most instructive to examine tomographic models of the bottom few hundred kilometres of the mantle, and specifically, in order to distinguish thermal from chemical or mineralogical variations, then models of at least two independent seismic parameters (i.e.  $V_P$ ,  $V_S$  or density) are required, at the same spatial resolution. Conventionally, tomographic data are presented as maps of lateral variations in sound speed and density with respect to a reference model (e.g. Fig. 13.10). These red-and-blue maps give a clear visual display of “fast” and “slow” regions with respect to the reference model, but details of the distributions of seismic velocities are lost due to the essentially binary parameterisation of seismic structure. Another way of analysing the models is to compile histograms of the frequency at which each value of a velocity perturbation occurs at a given depth (e.g. Deschamps and Trampert 2003; Hernlund and Houser 2008). Histograms showing the global distributions of  $P$  velocity perturbations ( $d\ln V_P$ ) and  $S$  velocity perturbations ( $d\ln V_S$ ) with respect to PREM (Dziewonski and Anderson 1981) at 2741 km and 2981 km depth (Mosca 2010) are shown in Fig. 13.11. The position and shape (i.e. width and skew) of these histograms are influenced by two factors: (1) the amplitude of any lateral variations in temperature and composition, and the frequency with which such variations occur and (2) errors and uncertainties in the tomographic model used to construct the histograms. Assuming that the second factor is sufficiently small relative to the first factor, we can use the histograms to place constraints on the thermo-chemical variations which are present at a given depth.

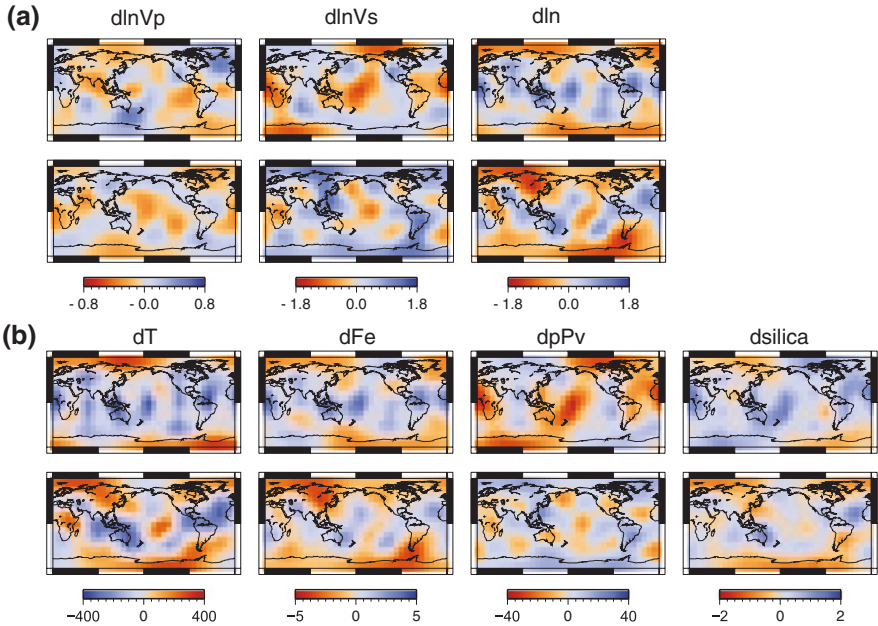


**Fig. 13.10** **a** Maps of  $d\ln V_P$ ,  $d\ln V_S$  and  $d\ln \rho$  at 2600 km (*upper row*) and 2891 km (*lower row*) with respect to PREM, inferred from joint inversion of normal modes and body waves by Mosca et al. (2012). Mosca et al. used the neighbourhood algorithm to derive probability density functions (*pdfs*) of the seismic structure at  $15^\circ$  intervals; the maps here display the mean of each *pdf*. Only the seismic structure corresponding to even spherical harmonic degrees 0, 2, 4 and 6 was calculated. **b** Conversion of seismic structure into probabilistic maps of temperature, iron, post-perovskite and silicate variations at 2600 km (*upper row*) and 2891 km (*lower row*) by Mosca et al. (2012) using the Metropolis–Hastings algorithm (Mosegaard and Tarantola 1995). *pdfs* of the thermo-chemical structure were calculated at  $15^\circ$  intervals; the maps show the mean of each *pdf* within a given  $15^\circ$  bin.  $dFe$  refers to the volumetric change in iron-bearing minerals ( $FeSiO_3$ ) perovskite and post-perovskite and  $FeO$  wüstite.  $dsilica$  refers to the volumetric change in Si-bearing minerals ( $Mg, Fe$ ) $SiO_3$  perovskite and post-perovskite,  $CaSiO_3$  calcium perovskite, and free  $SiO_2$ .  $dpPv$  refers to the percentage change in pPv within the ( $Mg, Fe$ ) $SiO_3$  perovskite and post-perovskite phases. Note that at 2600 km, the seismic reference model contains  $\sim 67 \pm 20\%$  pPv, while at 2891 km, it contains  $63 \pm 23\%$  pPv (see Fig. 13 in Mosca et al. 2012)

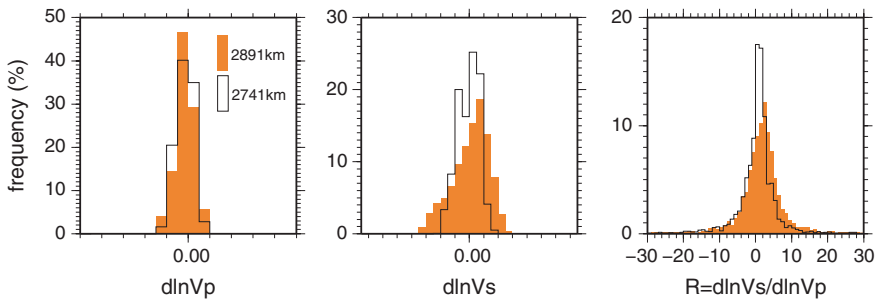


**Fig. 13.11** Histograms showing the frequency distributions of lateral variations of  $V_P$  ( $d\ln V_P$ ),  $V_S$  ( $d\ln V_S$ ) and seismic parameter  $R = d\ln V_P/d\ln V_S$  at two depths near the CMB, calculated from a global compilation of  $P$  and  $S$  wave travel times by Mosca (2010) using the path average approximation (Mosca and Trampert 2009)

The histograms in Fig. 13.11 were generated from body wave travel time observations (Ritsema and van Heijst 2002) using a procedure known as the path average approximation (Mosca and Trampert 2009). This approximation allows us to map lateral velocity perturbations within a narrow depth interval (narrower than conventional tomography) but with a correspondingly large uncertainty. By benchmarking the travel time anomalies given by the path average approximation against those generated by the more conventional ray and finite-frequency theory, the standard deviation of these uncertainties can be estimated (Mosca and Trampert 2009). Thereafter, for any thermo-chemical modelling aimed at fitting the histograms in Fig. 13.11, we can apply a correction to the synthetic models which takes into account the seismic uncertainties of the real data. This makes comparison between seismic data and thermo-chemical structures more consistent.

The path average approximation (PAVA) for body waves is most appropriate when the ray paths have a global coverage with no azimuthal bias and a tightly constrained turning depth. In this respect,  $P$  and  $S$  waves that diffract along the CMB ( $P_{\text{diff}}$  and  $S_{\text{diff}}$ ) are ideal, because we know that they bottom at the CMB, and data are available with a global coverage (Ritsema and van Heijst 2002). Furthermore, the PAVA becomes more accurate the longer the waves spend at their turning depth, and  $P$  and  $S$  diffracted waves can travel long distances along the CMB before returning to shallower mantle. In Cobden et al. (2012), we attempted to construct sets of thermo-chemical variations which would reproduce the global distributions of  $\text{dln}V_P$ ,  $\text{dln}V_S$  and  $R = \text{dln}V_P/\text{dln}V_S$  obtained from  $P_{\text{diff}}$  and  $S_{\text{diff}}$  arrivals (Fig. 13.11, 2891 km). In this paper, we also show results from similar calculations performed for  $P$  and  $S$  waves with bottoming depth of  $\sim 2741$  km (Fig. 13.11, 2741 km). The uncertainty in the ray turning depth is greater at this depth (a slowness range of  $\pm 0.5$  s/deg is used) than at the CMB, and the ray coverage is also less dense, so the contribution of seismic uncertainties to the histograms is greater. At shallower depths than this, the ray coverage becomes too biased to represent the global structure so no thermo-chemical modelling is undertaken.

For each of the two depths considered, the seismic velocities corresponding to a given thermo-chemical structure are calculated using the mineral elastic parameters and equation of state given in (Stixrude and Lithgow-Bertelloni 2005; Xu et al. 2008; Stixrude and Lithgow-Bertelloni 2011). In order to compute seismic derivatives  $\text{dln}V_P$  and  $\text{dln}V_S$ , we first generate a set of “reference models”, whose temperature and mineralogy are chosen at random within broad but pre-defined ranges (see Cobden et al. 2012 for details), of which only those whose seismic properties fit PREM to within 1 % are retained (since this was the reference model used in the real seismic data). For each retained reference model, we then generate an associated “perturbed model”, whose temperature and mineralogy are again chosen at random. We assume that the finite difference in  $V_P$  and  $V_S$  between the reference and perturbed model is approximately equal to  $\text{dln}V_P$  and  $\text{dln}V_S$ . We compute sets of up to 800,000 initial reference and perturbed model pairs and thus 800,000 values of  $\text{dln}V_P$  and  $\text{dln}V_S$  from which we can construct histograms of their frequency distribution. Although the seismic properties of the synthetic

models follow a much broader and more uniform distribution than the histograms in Fig. 13.11, due to the broad range of permitted thermo-chemical variations, a fitting procedure called the Metropolis–Hastings algorithm (Mosegaard and Tarantola 1995) can be used to extract a subset of these models which fit the frequency distributions of the real seismic data as closely as possible. Immediately prior to performing the Metropolis–Hastings (M-H) algorithm, seismic uncertainties following a normal distribution, with a standard deviation given by the uncertainty of the PAVA at that depth, are added to the synthetic seismic velocities.

We produced several different sets of 800,000 models. In one set, we specified that no post-perovskite should be present, and in another set, we allowed a mixture of both perovskite and post-perovskite. At the CMB, we also created a set of models in which no perovskite was present. We then compared the relative fit of the different sets to the histograms of Fig. 13.11. Although with all of the sets of models, it is possible to extract a subset which reproduces the real data histograms to more than 90 %, when we studied the seismic uncertainties of the accepted models, we found significant biases in the uncertainties of the “no post-perovskite” models. (Fig. 13.12a) Ideally, if a set of thermo-chemical models is fitting the seismic data due to its underlying thermo-chemical properties, then the mean of the uncertainties should be 0, since this was the mean of the uncertainties before data fitting. For the “no post-perovskite” models at 2891 km, the mean of the uncertainties is shifted by more than half a standard deviation towards negative values in  $\ln V_P$  and positive values in  $\ln V_S$  (Fig. 13.12a). At 2741 km, the bias in the uncertainties is still present, although the effect is smaller. For models containing a mixture of Pv and pPv, the uncertainties are much less biased, and at 2891 km, no significant difference can be seen for models which contain a mixture of Pv and pPv and models which contain no Pv. This result can be taken as an indication that a pPv-bearing CMB region fits the seismic data better than a pPv-free one.

For models in which both Pv and pPv were present, we allowed the percentage of pPv in the reference models to vary randomly between 0 and 100 %. The pPv contents for those (reference) models which were accepted by the M-H algorithm are shown in Fig. 13.12b. At 2891 km, the distribution has a strong negative skew with a peak at 75–80 % pPv. At 2741 km, the skew is weaker and the modal histogram bin is at 65–70 % pPv. The fact that most models favour a large percentage of pPv to be present is supportive of the hypothesis that a significant amount of pPv is present within  $D''$ . The fact that the distribution becomes more uniform at 2741 km compared to 2891 km, with a peak at a lower percentage of pPv, taken together with a smaller misfit of the  $P$  and  $S$  velocity uncertainties (Fig. 13.12a), is consistent with having a lower overall amount of pPv at a depth of 2741 km than at 2891 km. We find that it is particularly difficult to generate models which fit PREM within 1 % at 2891 km when there is zero or little post-perovskite, because the elastic parameters of the other minerals present favour very low temperatures (c. 2000 K) which are unlikely to occur near the CMB.

A related study by Mosca et al. (2012) combined body wave travel times with normal mode observations to generate a probabilistic tomography model of the lowermost mantle (Fig. 13.10). The inclusion of normal modes provides

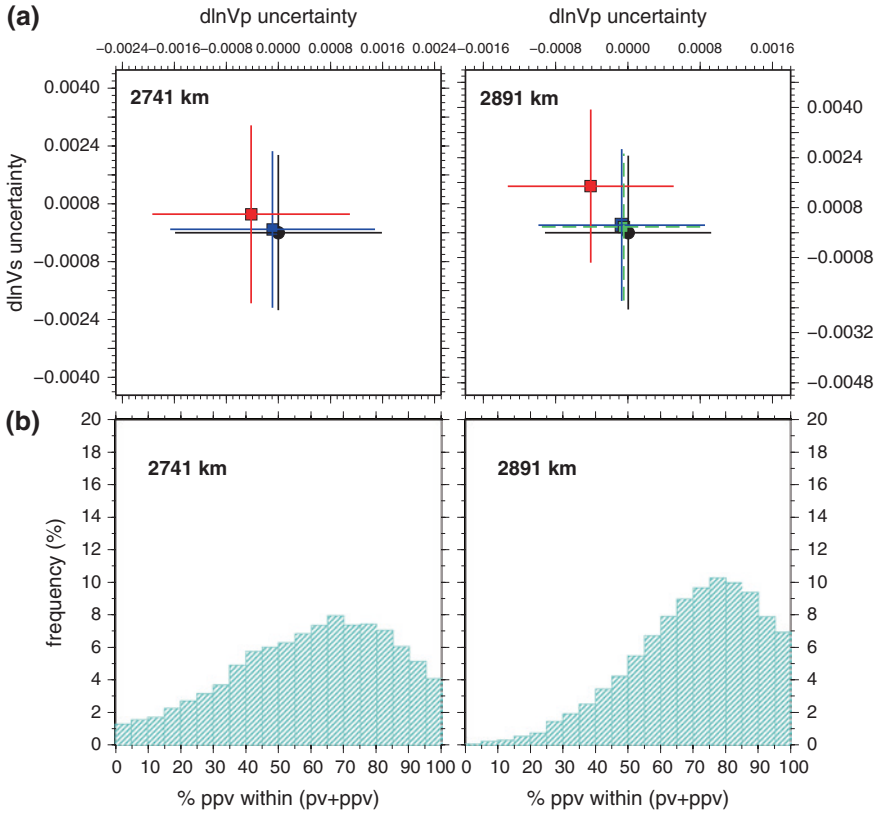


**Fig. 13.12** **a** Means (*squares*) and standard deviations (*lines*) of seismic uncertainties of thermochemical models. *Black* uncertainty distribution before applying Metropolis–Hastings algorithm. *Colours* uncertainty distribution of accepted models after M–H. *Blue* Pv and pPv present; *red* no pPv present; *green* no Pv present. **b** Distribution of %pPv in the reference models used to generate seismic derivatives, which fit PREM within 1 % and are accepted by the M–H algorithm. %pPv refers to the volumetric percentage of pPv within the (Mg, Fe)SiO<sub>3</sub> perovskite and post-perovskite phases

constraints on the density structure  $\rho$  in addition to  $V_P$  and  $V_S$ . Using the M–H algorithm, Mosca et al. (2012) converted the probability density functions (*pdfs*) of  $V_P$ ,  $V_S$  and  $\rho$  at each node of the tomography model into *pdfs* of temperature, iron, pPv and silicate variations, with the mean of the *pdfs* being indicative of the most likely value of  $dT$ ,  $dFe$ ,  $dpPv$  and  $dsilicate$  at each node (Fig. 13.10b). Mosca et al. found that the mean degree 0 structure of the models fitting the seismic data *pdfs* contained 67 % pPv at 2819 km (with a standard deviation of 20 %) and 63 % pPv (with standard deviation 23 %) at 2600 km. Given that the calculations involved a different data set (i.e. normal modes) and slightly different depth parameterisation than the PAVA calculations, these results are reasonably consistent with the PAVA calculations and again show a slight decrease in the total amount of pPv near the top of D'' compared to next to the CMB.

### 13.3.3.2 Lateral Variations in Post-perovskite Content

At 2891 km, we performed a simple cluster analysis (Sparks 1973) of the  $P_{\text{diff}}$  and  $S_{\text{diff}}$  travel time perturbations as a function of latitude and longitude, to divide the Earth into 4 regions possessing similar seismic characteristics (Cobden et al. 2012). One region corresponded to the position of the two large low-shear wave velocity provinces (LLSVP) under Africa and the Pacific and another correlated with fast circum-Pacific regions associated with subducted slabs. We found that in all four regions, “no post-perovskite” mantle models had a greater misfit to the seismic data than post-perovskite-bearing models, and thus, with this method, we could not detect a preference for post-perovskite to be located in a particular geographic area (such as inside or outside the LLSVPs). The tomography models of Mosca et al. (2012), however, do provide insights into the likely lateral variations of pPv content, at 2600 and 2891 km (Fig. 13.10b). These probabilistic maps show that lateral variations in pPv content correlate strongly with  $\text{dln}V_s$ , but less so with  $\text{dln}V_p$  or density. At 2600 km, dpPv is most positive (and hence the total volume of pPv most likely to be highest) in the northwest and eastern margins of the Pacific, including the Caribbean, as well as throughout most of Eurasia and the Indian Ocean. dpPv is most negative (i.e. the total amount of pPv is most likely to be lowest) in the central and south-west Pacific, and beneath Africa. At 2891 km, the amplitude of negative variations decreases, but the pattern of positive and negative variations becomes more complex.

The patterns of pPv variations at 2600 km are very broadly compatible with observations of VTI anisotropy ( $V_{\text{sh}} > V_{\text{sv}}$ ) in the circum-Pacific (Sect. 13.3.2), and the idea that post-perovskite is most likely to be found in subducted slabs (whereby the anisotropy arises from slab deformation). That the two sets of observations do not agree exactly is not surprising when differences in the spatial resolution and parameterisation between regional anisotropy studies and global tomography inversions are taken into account. In particular, the tomography study of Mosca et al. (2012) inverts only for the even spherical harmonic degrees, 0, 2, 4 and 6, while at the same time, the structure is averaged vertically over depth intervals of  $\sim 300$  km. In future, inclusion of odd degrees and a finer depth resolution could allow a closer comparison between regional and global seismic studies.

Post-perovskite has been predicted to be most abundant in slabs due to their colder temperature—the positive Clapeyron slope of the phase transition could restrict pPv to only the colder parts of the  $D''$  region (e.g. Wookey et al. 2005b). Yet, in the models of Mosca et al. (2012), the correlation between dT and dpPv is positive instead of negative. This could be indicative of a more dominant influence by chemistry than temperature on the appearance of pPv inside the Earth (although at the same time, dpPv does not correlate strongly with dFe). However, it is worth noting that one of the main restrictions of the modelling procedure of both Cobden et al. (2012) and Mosca et al. (2012) is that mineral abundances are varied randomly with no imposed phase equilibria. Thus, it is possible (and indeed likely) that we generated thermo-chemical combinations which are not thermodynamically stable. On the other hand, as we showed in Sect. 13.2.1, it is not meaningful

to impose phase equilibria, when the structure of the Pv–pPv phase boundary remains so highly unconstrained, and doing so will simply force the solution towards a biased answer which does not reflect the full uncertainty of the model. Furthermore, the existence of mechanical mixtures of different compositions (Xu et al. 2008) could produce bulk mineralogies which would not actually be thermodynamically stable as a uniform assemblage. The results presented in this section rely additionally on the accuracy of the assumed mineral elastic parameters. We have used one of the most comprehensive and self-consistent data sets currently available (Stixrude and Lithgow-Bertelloni 2011), but some of the parameters are not yet tightly constrained by experiments (e.g. shear velocities of post-perovskite; see Sect. 13.2.3) and may change significantly in the future. While there is a chance that this could impact our interpretation, we do not anticipate major changes, since we have been working with velocity perturbations, which are several times less sensitive to changes in elastic parameters than absolute velocities.

### 13.3.4 Future Directions

The probes outlined in Sects. 13.3.1–13.3.3 have primarily been derived using classical methods (e.g. 1-D reflectivity forward modelling of waveform stacks for the seismic discontinuities and ray theory for the tomography models) which aim to fit the timing, amplitude or polarity of specific wave phases. A more accurate, but computationally demanding, approach is to reconstruct the entire seismic waveform, i.e. full-waveform inversion. This approach has the advantage that weak or overlapping phases, which are difficult to observe with classical methods, are included in the analysis, and subjective data-picking errors are avoided. For example, in traditional discontinuity studies of PdP and SdS phases, there may be a bias towards observing velocity increases over decreases (Fig. 13.6, Gaherty and Lay 1992; Flores and Lay 2005) and towards accumulating the most observations in regions with the strongest amplitude reflections (Lay and Garnero 2011). While more complete descriptions of seismic wave propagation have been developed in recent years, including the computation of finite-frequency kernels (e.g. Montelli et al. 2004; Panning and Romanowicz 2006) and full-waveform inversions (e.g. Fichtner et al. 2010), for the lowermost mantle, these methods are still in the early stages of development (e.g. Fuji et al. 2012) and have not yet been used to map 3-D seismic structure. However, they have been used to construct regional 1-D profiles of the  $S$  wave speed within  $D''$  in regions of dense data coverage (e.g. Kawai et al. 2007a, b, 2010; Konishi et al. 2009; Kawai and Geller 2010; Konishi et al. 2012). These 1-D profiles are inevitably smooth and oscillatory in appearance and cannot distinguish sharp discontinuities from gradual changes in wave speed. They are qualitatively consistent with discontinuity studies (Sect. 13.3.1) in that they tend to show an increase in  $S$  wave speed  $\sim 200$ – $400$  km above the CMB, which is broadly compatible with a phase change from perovskite to post-perovskite. In order to be diagnostic of the presence or absence of post-perovskite,

and with no information about the sharpness of the  $S$  wave speed changes, then in future, additional information about the  $P$  wave speed structure or the density structure is required, preferably in three dimensions.

## 13.4 Conclusions

We have seen that a wide range of seismic observations on different length scales are compatible with the presence of post-perovskite inside the Earth and with the hypothesis that the  $D''$  discontinuity is (at least partially) associated with a phase change from perovskite to post-perovskite. Although every set of seismic observations has significant uncertainties, and although a compatibility between seismic observations and the physical properties of post-perovskite does not exclude all other physical explanations for the seismic structure, the fact that multiple data types and data inversions can be reconciled with the existence of post-perovskite, in some cases more readily than without post-perovskite, provides a strong case that the mineral is indeed present in the lowermost mantle. We anticipate that in seismology, multi-azimuthal studies of anisotropy will play an important role in further constraining deep mantle mineralogical structures, while full-waveform inversion methods may eventually have the capacity to image 3-D seismic structures in  $D''$  at high resolution. In mineral physics, the phase equilibria between perovskite and post-perovskite are, at present, controversial. However, we expect that with the accumulation of more data, in particular, investigations of mixed-phase assemblages and calibration of the rate of conversion of Pv to pPv with increasing pressure, we will eventually converge on a consistent model of the phase equilibria, which can be applied directly to seismic observations.

**Acknowledgments** The authors thank Nobuaki Fuji and Frédéric Deschamps for helpful comments which improved the manuscript. This work was partially funded by the DFG (German Research Foundation) on grant number TH1530/5-1 and the NWO (Dutch Science Foundation) on grant number NWO: VIDI 864.11.008.

## References

- Akahama Y, Kawamura H (2004) High-pressure Raman spectroscopy of diamond anvils to 250 GPa: method for pressure determination in the multimegabar pressure range. *J Appl Phys* 96:3748–3751
- Akahama Y, Kawamura H, Singh A (2002) Equation of state of bismuth to 222 GPa and comparison of gold and platinum pressure scales to 145 GPa. *J Appl Phys* 92:5892–5897
- Akber-Knutson S, Steinle-Neumann G, Asimow PD (2005) Effect of Al on the sharpness of the  $\text{MgSiO}_3$  perovskite to post-perovskite phase transition. *Geophys Res Lett* 32:L14303
- Ammann MW, Brodholt JP, Wookey J, Dobson DP (2010) First-principles constraints on diffusion in lower-mantle minerals and a weak  $D''$  layer. *Nature* 465:462–465
- Anderson OL, Isaak DG, Yamamoto S (1989) Anharmonicity and the equation of state for gold. *J Appl Phys* 65:1534–1543

- Andraut D, Munoz M, Bolfan-Casanova N, Guignot N, Perrillat J, Aquilanti G, Pascarelli S (2010) Experimental evidence for perovskite and post-perovskite coexistence throughout the whole D'' region. *Earth Planet Sci Lett* 293:90–96
- Asanuma H, Ohtani E, Sakai T, Terasaki H, Kamada S, Kondo T, Kikegawa T (2010) Melting of iron-silicon alloy up to the core-mantle boundary pressure: implications to the thermal structure of the Earth's core. *Phys Chem Miner* 37:353–359
- Avants M, Lay T, Russell S, Garnero E (2006) Shear velocity variation within the D'' region beneath the central Pacific. *J Geophys Res Solid Earth* 111:B05305
- Baumgardt DR (1989) Evidence for a P-wave velocity anomaly in D''. *Geophys Res Lett* 16:657–660
- Beghein C, Trampert J, van Heijst HJ (2006) Radial anisotropy in seismic reference models of the mantle. *J Geophys Res Solid Earth* 111:B02303
- Bullen KE (1950) An earth model based on a compressibility-pressure hypothesis. *Geophys J Int* 6:50–59
- Cammarano F, Goes S, Deuss A, Giardini D (2005) Is a pyrolytic adiabatic mantle compatible with seismic data? *Earth Planet Sci Lett* 232:227–243
- Campbell AJ, Seagle CT, Heinz DL, Shen G, Prakapenka VB (2007) Partial melting in the iron-sulfur system at high pressure: a synchrotron X-ray diffraction study. *Phys Earth Planet Inter* 162:119–128
- Caracas R, Cohen RE (2005a) Effect of chemistry on the stability and elasticity of the perovskite and post-perovskite phases in the MgSiO<sub>3</sub>-FeSiO<sub>3</sub>-Al<sub>2</sub>O<sub>3</sub> system and implications for the lowermost mantle. *Geophys Res Lett* 32:L16310
- Caracas R, Cohen R (2005b) Prediction of a new phase transition in Al<sub>2</sub>O<sub>3</sub> at high pressures. *Geophys Res Lett* 32:L06303
- Catalli K, Shim S, Prakapenka V (2009) Thickness and Clapeyron slope of the post-perovskite boundary. *Nature* 462:782–785
- Chaloner JW, Thomas C, Rietbrock A (2009) P- and S-wave reflectors in D' beneath southeast Asia. *Geophys J Int* 179:1080–1092
- Chambers K, Woodhouse JH (2006) Transient D'' discontinuity revealed by seismic migration. *Geophys Res Lett* 33:L17312
- Christensen UR (1989) Models of mantle convection—one or several layers. *Philos Trans R Soc Lond Ser A Math Phys Eng Sci* 328:417–424
- Christensen UR, Hofmann AW (1994) Segregation of subducted oceanic-crust in the convecting mantle. *J Geophys Res Solid Earth* 99:19867–19884
- Cobden L, Thomas C (2013) The origin of D' reflections: a systematic study of seismic array data sets. *Geophys J Int* 194:1091–1118
- Cobden L, Goes S, Ravenna M, Styles E, Cammarano F, Gallagher K, Connolly JAD (2009) Thermochemical interpretation of 1-D seismic data for the lower mantle: the significance of nonadiabatic thermal gradients and compositional heterogeneity. *J Geophys Res Solid Earth* 114:B11309
- Cobden L, Mosca I, Trampert J, Ritsema J (2012) On the likelihood of post-perovskite near the core-mantle boundary: a statistical interpretation of seismic observations. *Phys Earth Planet Inter* 210:21–35
- Cococcioni M, de Gironcoli S (2005) Linear response approach to the calculation of the effective interaction parameters in the LDA + U method. *Phys Rev B* 71:035105
- Davies GF, Gurnis M (1986) Interaction of mantle dregs with convection: lateral heterogeneity at the core mantle boundary. *Geophys Res Lett* 13:1517–1520
- Davies D, Kelly E, Filson J (1971) Vespa process for analysis of seismic signals. *Nat Phys Sci* 232:8–13
- Davis JP, Weber M (1990) Lower mantle velocity inhomogeneity observed at GRF array. *Geophys Res Lett* 17
- Deschamps F, Trampert J (2003) Mantle tomography and its relation to temperature and composition. *Phys Earth Planet Inter* 140:277–291

- Dewaele A, Loubeyre P, Mezouar M (2004) Equations of state of six metals above 94 GPa. *Phys Rev B* 70:094112
- Ding X, Helmberger D (1997) Modelling  $D''$  structure beneath Central America with broadband seismic data. *Phys Earth Planet Inter* 101:245–270
- Dziewonski AM, Anderson DL (1981) Preliminary reference earth model. *Phys Earth Planet Inter* 25:297–356
- Fei Y, Van Orman J, Li J, van Westrenen W, Sanloup C, Minarik W, Hirose K, Komabayashi T, Walter M, Funakoshi K (2004) Experimentally determined postspinel transformation boundary in  $Mg_2SiO_4$  using MgO as an internal pressure standard and its geophysical implications. *J Geophys Res Solid Earth* 109:B02305
- Fei Y, Ricolleau A, Frank M, Miibe K, Shen G, Prakapenka V (2007) Toward an internally consistent pressure scale. *Proc Natl Acad Sci USA* 104:9182–9186
- Fichtner A, Kennett BLN, Igel H, Bunge H (2010) Full waveform tomography for radially anisotropic structure: new insights into present and past states of the Australasian upper mantle. *Earth Planet Sci Lett* 290:270–280
- Flores C, Lay T (2005) The trouble with seeing double. *Geophys Res Lett* 32:L24305
- Fouch M, Fischer K, Wyssession M (2001) Lowermost mantle anisotropy beneath the Pacific: imaging the source of the Hawaiian plume. *Earth Planet Sci Lett* 190:167–180
- Fuji N, Chevrot S, Zhao L, Geller RJ, Kawai K (2012) Finite-frequency structural sensitivities of short-period compressional body waves. *Geophys J Int* 190:522–540
- Gaherty JB, Lay T (1992) Investigation of laterally heterogeneous shear velocity structure in  $D''$  beneath Eurasia. *J Geophys Res Solid Earth* 97:417–435
- Garnero EJ, Lay T (1997) Lateral variations in lowermost mantle shear wave anisotropy beneath the north Pacific and Alaska. *J Geophys Res Solid Earth* 102:8121–8135
- Grand S (2002) Mantle shear-wave tomography and the fate of subducted slabs. *Philos Trans R Soc Lond Ser A Math Phys Eng Sci* 360:2475–2491
- Grocholski B, Catali K, Shim S, Prakapenka V (2012) Mineralogical effects on the detectability of the postperovskite boundary. *Proc Natl Acad Sci USA* 109:2275–2279
- Guignot N, Andrault D, Morard G, Bolfan-Casanova N, Mezouar M (2007) Thermoelastic properties of post-perovskite phase  $MgSiO_3$  determined experimentally at core-mantle boundary P-T conditions. *Earth Planet Sci Lett* 256:162–168
- Gutenberg B (1914) Über Erdbebenwellen. VII A Beobachtungen an Registrierungen von Fernbeben in Göttingen und Folgerungen über die Konstitution des Erdkörpers. *Nachr d K Ges d Wiss zu Göttingen, Math Phys Klasse* 125–177
- Hernlund JW, Houser C (2008) The statistical distribution of seismic velocities in Earth's deep mantle. *Earth Planet Sci Lett* 265:423–437
- Hernlund JW, Thomas C, Tackley PJ (2005) A doubling of the post-perovskite phase boundary and structure of the Earth's lowermost mantle. *Nature* 434:882–886
- Hirose K (2006) Postperovskite phase transition and its geophysical implications. *Rev Geophys* 44:RG3001
- Hirose K, Takafuji N, Sata N, Ohishi Y (2005) Phase transition and density of subducted MORB crust in the lower mantle. *Earth Planet Sci Lett* 237:239–251
- Hirose K, Sinmyo R, Sata N, Ohishi Y (2006) Determination of post-perovskite phase transition boundary in  $MgSiO_3$  using Au and MgO pressure standards. *Geophys Res Lett* 33:L01310
- Hirose K, Sata N, Komabayashi T, Ohishi Y (2008a) Simultaneous volume measurements of Au and MgO to 140 GPa and thermal equation of state of Au based on the MgO pressure scale. *Phys Earth Planet Inter* 167:149–154
- Hirose K, Takafuji N, Fujino K, Shieh SR, Duffy TS (2008b) Iron partitioning between perovskite and post-perovskite: a transmission electron microscope study. *Am Mineral* 93:1678–1681
- Hirose K, Nagaya Y, Merkel S, Ohishi Y (2010) Deformation of  $MnGeO_3$  post-perovskite at lower mantle pressure and temperature. *Geophys Res Lett* 37:L20302
- Holmes NC, Moriarty JA, Gathers GR, Nellis WJ (1989) The equation of state of platinum to 660 gpa (6.6 mbar). *J Appl Phys* 66:2962–2967

- Houard S, Nataf HC (1992) Further evidence for the lay discontinuity beneath northern Siberia and the North-Atlantic from short-period P-waves recorded in France. *Phys, Earth Planet Inter* 72
- Houard S, Nataf HC (1993) Laterally varying reflector at the top of D'' beneath northern Siberia. *Geophys J Int* 115
- Houser C (2007) Constraints on the presence or absence of post-perovskites in the lower mantle from long-period seismology. In: Hirose K, Brodholt JP, Lay T, Yuen DA (eds) *Post-perovskite: the last mantle phase transition*, vol 174. American Geophysical Union, Washington D.C., pp 191–216
- Hunt SA, Weidner DJ, Li L, Wang L, Walte NP, Brodholt JP, Dobson DP (2009) Weakening of calcium iridate during its transformation from perovskite to post-perovskite. *Nat Geosci* 2:794–797
- Hutko A, Lay T, Garnero E, Revenaugh J (2006) Seismic detection of folded, subducted lithosphere at the core-mantle boundary. *Nature* 441:333–336
- Hutko AR, Lay T, Revenaugh J, Garnero EJ (2008) Anticorrelated seismic velocity anomalies from post-perovskite in the lowermost mantle. *Science* 320:1070–1074
- Hutko AR, Lay T, Revenaugh J (2009) Localized double-array stacking analysis of PcP: D'' and ULVZ structure beneath the Cocos plate, Mexico, central Pacific, and north Pacific. *Phys Earth Planet Inter* 173:60–74
- Iitaka T, Hirose K, Kawamura K, Murakami M (2004) The elasticity of the MgSiO<sub>3</sub> post-perovskite phase in the Earth's lowermost mantle. *Nature* 430:442–445
- Ishii M, Tromp J (1999) Normal-mode and free-air gravity constraints on lateral variations in velocity and density of Earth's mantle. *Science* 285:1231–1236
- Jamieson JC, Fritz JN, Manghnani MH (1982) Pressure measurements at high temperature in X-ray diffraction studies: gold as a primary standard. In: Akimoto S, Manghnani Murli H (eds) *High-pressure research in geophysics*. Centre for Academic Publications Japan, Tokyo, pp 27–48
- Kamada S, Terasaki H, Ohtani E, Sakai T, Kikegawa T, Ohishi Y, Hirao N, Sata N, Kondo T (2010) Phase relationships of the Fe-FeS system in conditions up to the Earth's outer core. *Earth Planet Sci Lett* 294:94–100
- Kaneshima S, Helffrich G (1999) Dipping low-velocity layer in the mid-lower mantle: evidence for geochemical heterogeneity. *Science* 283:1888–1891
- Kawai K, Geller RJ (2010) Waveform inversion for localized seismic structure and an application to D'' structure beneath the Pacific. *J Geophys Res Solid Earth* 115:B01305
- Kawai K, Tsuchiya T (2009) Temperature profile in the lowermost mantle from seismological and mineral physics joint modeling. *Proc Natl Acad Sci USA* 106:22119–22123
- Kawai K, Geller RJ, Fuji N (2007a) D'' beneath the Arctic from inversion of shear waveforms. *Geophys Res Lett* 34:L21305
- Kawai K, Takeuchi N, Geller RJ, Fuji N (2007b) Possible evidence for a double crossing phase transition in D'' beneath Central America from inversion of seismic waveforms. *Geophys Res Lett* 34:L09314
- Kawai K, Geller RJ, Fuji N (2010) Waveform inversion for S-wave structure in the lowermost mantle beneath the Arctic: Implications for mineralogy and chemical composition. *Geophys Res Lett* 37:L16301
- Kendall J, Nangini C (1996) Lateral variations in D'' below the Caribbean. *Geophys Res Lett* 23:399–402
- Kendall JM, Silver PG (1998) Investigating causes of D'' anisotropy. In: Gurnis M, Wyssession ME, Knittle E, Buffet BA (eds) *The core-mantle boundary region*. American Geophysical Union, Washington D.C., pp 97–118
- Kennett B, Engdahl E, Buland R (1995) Constraints on seismic velocities in the Earth from travel-times. *Geophys J Int* 122:108–124
- Kesson S, Fitz Gerald J, Shelley J (1998) Mineralogy and dynamics of a pyrolite lower mantle. *Nature* 393:252–255
- Kito T, Rost S, Thomas C, Garnero EJ (2007) New insights into the P- and S-wave velocity structure of the D'' discontinuity beneath the Cocos plate. *Geophys J Int* 169:631–645

- Knittle E, Jeanloz R (1987) Synthesis and equation of state of (Mg, Fe) $\text{SiO}_3$  perovskite to over 100 gigapascals. *Science* 235:668–670
- Knittle E, Jeanloz R (1989) Simulating the core-mantle boundary—an experimental-study of high-pressure reactions between silicates and liquid-iron. *Geophys Res Lett* 16:609–612
- Kobayashi Y, Kondo T, Ohtani E, Hirao N, Miyajima N, Yagi T, Nagase T, Kikegawa T (2005) Fe-Mg partitioning between (Mg, Fe) $\text{SiO}_3$  post-perovskite, perovskite, and magnesiowüstite in the Earth's lower mantle. *Geophys Res Lett* 32:L19301
- Konishi K, Kawai K, Geller RJ, Fuji N (2009) MORB in the lowermost mantle beneath the western Pacific: evidence from waveform inversion. *Earth Planet Sci Lett* 278:219–225
- Konishi K, Kawai K, Geller RJ, Fuji N (2012) Waveform inversion of broad-band body wave data for the S-velocity structure in the lowermost mantle beneath the Indian subcontinent and Tibetan Plateau. *Geophys J Int* 191:305–316
- Kubo A, Kiefer B, Shim S, Shen G, Prakapenka VB, Duffy TS (2008) Rietveld structure refinement of MgGeO $_3$  post-perovskite phase to 1 Mbar. *Am Mineral* 93:965–976
- Kustowski B, Ekstrom G, Dziewonski AM (2008) Anisotropic shear-wave velocity structure of the Earth's mantle: a global model. *J Geophys Res Sol Earth* 113:B06306
- Lay T (2008) Sharpness of the D'' discontinuity beneath the Cocos plate: implications for the perovskite to post-perovskite phase transition. *Geophys Res Lett* 35:L03304
- Lay T, Garnero E (2004) Core-mantle boundary structures and processes. In: Sparkes RSJ, Hawkesworth CJ (eds) *State of the planet: frontiers and challenges in geophysics*, vol 150. American Geophysical Union, Washington D.C., pp 25–41
- Lay T, Garnero EJ (2007) Reconciling the post-perovskite phase with seismological observations of lowermost mantle structure. In: Hirose K, Brodholt John, Lay Thorne, Yuen David (eds) *Post-perovskite: the last mantle phase transition*. American Geophysical Union, Washington D.C., pp 129–153
- Lay T, Garnero EJ (2011) Deep mantle seismic modeling and imaging. *Annu Rev Earth Planet Sci* 39(39):91–123
- Lay T, Helmberger D (1983) A lower mantle S-wave triplication and the shear velocity structure of D''. *Geophys J Roy Astron Soc* 75:799–837
- Lay T, Young CJ (1991) Analysis of seismic SV waves in the cores penumbra. *Geophys Res Lett* 18:1373–1376
- Lay T, Garnero E, Russell S (2004) Lateral variation of the D'' discontinuity beneath the Cocos plate. *Geophys Res Lett* 31:L15612
- Lay T, Hernlund J, Garnero EJ, Thorne MS (2006) A post-perovskite lens and D'' heat flux beneath the central Pacific. *Science* 314:1272–1276
- Long MD (2009) Complex anisotropy in D'' beneath the eastern Pacific from SKS-SKKS splitting discrepancies. *Earth Planet Sci Lett* 283:181–189
- Mao WL, Shen G, Prakapenka V, Meng Y, Campbell A, Heinz D, Shu J, Hemley R, Mao H (2004) Ferromagnesian postperovskite silicates in the D'' layer of the Earth. *Proc Natl Acad Sci USA*. 101:15867–15869
- Mao WL et al (2005) Iron-rich silicates in the Earth's D'' layer. *Proc Natl Acad Sci USA* 102
- Mao WL, Meng Y, Mao H (2010) Elastic anisotropy of ferromagnesian post-perovskite in Earth's D'' layer. *Phys Earth Planet Inter* 180:203–208
- Masters G, Laske G, Bolton H, Dziewonski AM (2000) The relative behaviour of shear velocity, bulk sound speed, and compressional velocity in the mantle: implications for chemical and thermal structure. In: Karato S, Forte A, Liebermann R, Masters G, Stixrude L (eds) *Earth's deep interior: mineral physics and tomography from the atomic to the global scale*, vol 117. American Geophysical Union, Washington D.C., pp 63–87
- Matzel E, Sen MK, Grand SP (1996) Evidence for anisotropy in the deep mantle beneath Alaska. *Geophys Res Lett* 23:2417–2420
- Maupin V, Garnero EJ, Lay T, Fouch MJ (2005) Azimuthal anisotropy in the D'' layer beneath the Caribbean. *J Geophys Res Solid Earth* 110:B08301
- McNamara AK, Zhong SJ (2005) Thermochemical structures beneath Africa and the Pacific Ocean. *Nature* 437

- Meade C, Mao HK, Hu JZ (1995) High-temperature phase-transition and dissociation of (Mg, Fe)SiO<sub>3</sub> perovskite at lower mantle pressures. *Science* 268:1743–1745
- Merkel S, McNamara AK, Kubo A, Speziale S, Miyagi L, Meng Y, Duffy TS, Wenk H (2007) Deformation of (Mg, Fe)SiO<sub>3</sub> post-perovskite and D anisotropy. *Science* 316:1729–1732
- Metsue A, Tsuchiya T (2012) Thermodynamic properties of (Mg, Fe<sub>2+</sub>)SiO<sub>3</sub> perovskite at the lower-mantle pressures and temperatures: an internally consistent LSDA + U study. *Geophys J Int* 190:310–322
- Metsue A, Tsuchiya T (2013) Shear response of Fe-bearing MgSiO<sub>3</sub> post-perovskite at lower mantle pressures. *Proc Jpn Acad Ser B Phys Biol Sci* 89:51–58
- Miyagi L, Nishiyama N, Wang Y, Kubo A, West DV, Cava RJ, Duffy TS, Wenk H (2008) Deformation and texture development in CaIrO<sub>3</sub> post-perovskite phase up to 6 GPa and 1300 K. *Earth Planet Sci Lett* 268:515–525
- Miyagi L, Kanitpanyacharoen W, Kaercher P, Lee KKM, Wenk H (2010) Slip systems in MgSiO<sub>3</sub> post-perovskite: implications for D'' anisotropy. *Science* 329:1639–1641
- Miyagi L, Kanitpanyacharoen W, Stackhouse S, Militzer B, Wenk H (2011) The enigma of post-perovskite anisotropy: deformation versus transformation textures. *Phys Chem Miner* 38:665–678
- Miyajima N, Ohgushi K, Ichihara M, Yagi T (2006) Crystal morphology and dislocation microstructures of CaIrO<sub>3</sub>: a TEM study of an analogue of the MgSiO<sub>3</sub> post-perovskite phase. *Geophys Res Lett* 33:L12302
- Montagner JP, Kennett BLN (1996) How to reconcile body-wave and normal-mode reference earth models. *Geophys J Int* 125:229–248
- Montelli R, Nolet G, Dahlen FA, Masters G, Engdahl ER, Hung SH (2004) Finite-frequency tomography reveals a variety of plumes in the mantle. *Science* 303:338–343
- Mosca I (2010) Probabilistic tomography using body wave, normal mode and surface wave data. PhD Thesis, Utrecht University, Utrecht
- Mosca I, Trampert J (2009) Path-average kernels for long wavelength traveltimes tomography. *Geophys J Int* 177:639–650
- Mosca I, Cobden L, Deuss A, Ritsema J, Trampert J (2012) Seismic and mineralogical structures of the lower mantle from probabilistic tomography. *J Geophys Res Solid Earth* 117:B06304
- Mosegaard K, Tarantola A (1995) Monte-carlo sampling of solutions to inverse problems. *J Geophys Res Solid Earth* 100:12431–12447
- Muirhead K, Datt R (1976) N-th root process applied to seismic array data. *Geophys J Roy Astron Soc* 47:197–210
- Murakami M, Hirose K, Kawamura K, Sata N, Ohishi Y (2004) Post-perovskite phase transition in MgSiO<sub>3</sub>. *Science* 304:855–858
- Murakami M, Hirose K, Sata N, Ohishi Y (2005) Post-perovskite phase transition and mineral chemistry in the pyrolytic lowermost mantle. *Geophys Res Lett* 32:L03304
- Murakami M, Sinogeikin SV, Bass JD, Sata N, Ohishi Y, Hirose K (2007) Sound velocity of MgSiO<sub>3</sub> post-perovskite phase: a constraint on the D'' discontinuity. *Earth Planet Sci Lett* 259:18–23
- Murakami M, Ohishi Y, Hirao N, Hirose K (2012) A perovskitic lower mantle inferred from high-pressure, high-temperature sound velocity data. *Nature* 485:90–94
- Nakagawa T, Tackley PJ (2011) Effects of low-viscosity post-perovskite on thermo-chemical mantle convection in a 3-D spherical shell. *Geophys Res Lett* 38:L04309
- Neuberg J, Wahr J (1991) Detailed investigation of a spot on the core mantle boundary using digital PcP data. *Phys Earth Planet Inter* 68:132–143
- Nishio-Hamane D, Fujino K, Seto Y, Nagai T (2007) Effect of the incorporation of FeAlO<sub>3</sub> into MgSiO<sub>3</sub> perovskite on the post-perovskite transition. *Geophys Res Lett* 34:L12307
- Niwa K, Yagi T, Ohgushi K, Merkel S, Miyajima N, Kikegawa T (2007) Lattice preferred orientation in CaIrO<sub>3</sub> perovskite and post-perovskite formed by plastic deformation under pressure. *Phys Chem Miner* 34:679–686
- Niwa K, Miyajima N, Seto Y, Ohgushi K, Gotou H, Yagi T (2012) In situ observation of shear stress-induced perovskite to post-perovskite phase transition in CaIrO<sub>3</sub> and the development of its deformation texture in a diamond-anvil cell up to 30 GPa. *Phys Earth Planet Inter* 194:10–17

- Nowacki A, Wookey J, Kendall J- (2010) Deformation of the lowermost mantle from seismic anisotropy. *Nature* 467:1091–1095
- Nowacki A, Wookey J, Kendall J- (2011) New advances in using seismic anisotropy, mineral physics and geodynamics to understand deformation in the lowermost mantle. *J Geodyn* 52:205–228
- Oganov AR, Ono S (2004) Theoretical and experimental evidence for a post-perovskite phase of  $\text{MgSiO}_3$  in Earth's  $D''$  layer. *Nature* 430:445–448
- Oganov A, Ono S (2005) The high-pressure phase of alumina and implications for Earth's  $D''$  layer. *Proc Natl Acad Sci USA* 102:10828–10831
- Oganov AR, Brodholt JP, Price GD (2002) Ab initio theory of phase transitions and thermoelasticity of minerals. In: Gramaccioli CM (ed) *Energy modelling in minerals*, vol 4, pp 83–170
- Ohta K, Hirose K, Sata N, Ohishi Y (2006) The sharpness and compositional effects on post-perovskite phase transition. *Geochim Cosmochim, Acta* 70
- Ohta K, Hirose K, Lay T, Sata N, Ohishi Y (2008) Phase transitions in pyrolite and MORB at lowermost mantle conditions: implications for a MORB-rich pile above the core-mantle boundary. *Earth Planet Sci Lett* 267:107–117
- Okada T, Yagi T, Niwa K, Kikegawa T (2010) Lattice-preferred orientations in post-perovskite-type  $\text{MgGeO}_3$  formed by transformations from different pre-phases. *Phys Earth Planet Inter* 180:195–202
- Ono S, Oganov AR (2005) In situ observations of phase transition between perovskite and  $\text{CaIrO}_3$ -type phase in  $\text{MgSiO}_3$  and pyrolytic mantle composition. *Earth Planet Sci Lett* 236
- Panning M, Romanowicz B (2004) Inferences on flow at the base of Earth's mantle based on seismic anisotropy. *Science* 303:351–353
- Panning M, Romanowicz B (2006) A three-dimensional radially anisotropic model of shear velocity in the whole mantle. *Geophys J Int* 167:361–379
- Reasoner C, Revenaugh J (1999) Short-period P wave constraints on  $D''$  reflectivity. *J Geophys Res Solid Earth* 104:955–961
- Ricard Y, Matern E, Matas J (2005) Synthetic tomographic images of slabs from mineral physics. In: van der Hilst RD, Bass Jay D, Matas Jan, Trampert J (eds) *Earth's deep mantle: structure, composition and evolution*, vol 160. American Geophysical Union, Washington D.C., pp 285–302
- Ringwood AE (1962) Model for upper mantle. *J Geophys Res* 67
- Ritsema J, van Heijst HJ (2002) Constraints on the correlation of P- and S-wave velocity heterogeneity in the mantle from P, PP, PPP and PKPab traveltimes. *Geophys J Int* 149:482–489
- Rokosky JM, Lay T, Garnero EJ (2006) Small-scale lateral variations in azimuthally anisotropic  $D''$  structure beneath the Cocos plate. *Earth Planet Sci Lett* 248:411–425
- Ross M, Mao HK, Bell PM, Xu JA (1986) The equation of state of dense argon—a comparison of shock and static studies. *J Chem Phys* 85:1028–1033
- Rost S, Thomas C (2002) Array seismology: methods and applications. *Rev Geophys* 40:1008
- Russell S, Reasoner C, Lay T, Revenaugh J (2001) Coexisting shear- and compressional-wave seismic velocity discontinuities beneath the central Pacific. *Geophys Res Lett* 28:2281–2284
- Sata N, Shen G, Rivers M, Sutton S (2002) Pressure-volume equation of state of the high-pressure B2 phase of NaCl. *Phys Rev B* 65:104114
- Saxena S, Dubrovinsky L, Lazor P, Cerenius Y, Haggkvist P, Hanfland M, Hu J (1996) Stability of perovskite ( $\text{MgSiO}_3$ ) in the Earth's mantle. *Science* 274:1357–1359
- Saxena S, Dubrovinsky L, Lazor P, Hu J (1998) In situ X-ray study of perovskite ( $\text{MgSiO}_3$ ): phase transition and dissociation at mantle conditions. *Eur J Mineral* 10:1275–1281
- Scherbaum F, Kruger F, Weber M (1997) Double beam imaging: mapping lower mantle heterogeneities using combinations of source and receiver arrays. *J Geophys Res Solid Earth* 102:507–522
- Schweitzer J, Fyen J, Mykkeltveit S, Kvaerna T (2002) Seismic arrays (Chap. 9). In: Bormann P (ed) *IASPEI new manual of seismological observatory practice*. GeoForschungszentrum, Potsdam
- Shieh S, Duffy T, Kubo A, Shen G, Prakapenka V, Sata N, Hirose K, Ohishi Y (2006) Equation of state of the postperovskite phase synthesized from a natural (Mg, Fe) $\text{SiO}_3$  orthopyroxene. *Proc Natl Acad Sci USA* 103:3039–3043

- Shieh SR, Dorfman SM, Kubo A, Prakapenka VB, Duffy TS (2011) Synthesis and equation of state of post-perovskites in the (Mg, Fe)<sub>3</sub>Al<sub>2</sub>Si<sub>3</sub>O<sub>12</sub> system. *Earth Planet Sci Lett* 312:422–428
- Shim S, Duffy T, Kenichi T (2002) Equation of state of gold and its application to the phase boundaries near 660 km depth in Earth's mantle. *Earth Planet Sci Lett* 203:729–739
- Shim SH, Duffy TS, Jeanloz R, Shen G (2004) Stability and crystal structure of MgSiO<sub>3</sub> perovskite to the core-mantle boundary. *Geophys Res Lett* 31:L10603
- Sidorin I, Gurnis M, Helmberger D, Ding X (1998) Interpreting D'' seismic structure using synthetic waveforms computed from dynamic models. *Earth Planet Sci Lett* 163:31–41
- Sidorin I, Gurnis M, Helmberger D (1999a) Dynamics of a phase change at the base of the mantle consistent with seismological observations. *J Geophys Res Solid Earth* 104:15005–15023
- Sidorin I, Gurnis M, Helmberger D (1999b) Evidence for a ubiquitous seismic discontinuity at the base of the mantle. *Science* 286:1326–1331
- Sinmyo R, Hirose K, Muto S, Ohishi Y, Yasuhara A (2011) The valence state and partitioning of iron in the Earth's lowermost mantle. *J Geophys Res Solid Earth* 116:B07205
- Sparks DN (1973) Euclidean cluster analysis. *J R Stat Soc Ser C Appl Stat* 126–130
- Speziale S, Zha C, Duffy T, Hemley R, Mao H (2001) Quasi-hydrostatic compression of magnesium oxide to 52 GPa: implications for the pressure-volume-temperature equation of state. *J Geophys Res Solid Earth* 106:515–528
- Stackhouse S, Brodholt JP (2007) High-temperature elasticity of MgSiO<sub>3</sub> post-perovskite. In: Hirose K, Brodholt JP, Lay T, Yuen D (eds) *Post-perovskite: the last mantle phase transition*, vol 174. American Geophysical Union, Washington D.C., pp 99–113
- Stackhouse S, Brodholt JP, Price GD (2005a) High temperature elastic anisotropy of the perovskite and post-perovskite Al<sub>2</sub>O<sub>3</sub>. *Geophys Res Lett* 32:L13305
- Stackhouse S, Brodholt JP, Wookey J, Kendall JM, Price GD (2005b) The effect of temperature on the seismic anisotropy of the perovskite and post-perovskite polymorphs of MgSiO<sub>3</sub>. *Earth Planet Sci Lett* 230:1–10
- Stackhouse S, Brodholt JP, Price GD (2006) Elastic anisotropy of FeSiO<sub>3</sub> end-members of the perovskite and post-perovskite phases. *Geophys Res Lett* 33:L01304
- Stixrude L, Lithgow-Bertelloni C (2005) Thermodynamics of mantle minerals—I. Physical properties. *Geophys J Int* 162:610–632
- Stixrude L, Lithgow-Bertelloni C (2011) Thermodynamics of mantle minerals—II. Phase equilibria. *Geophys J Int* 184:1180–1213
- Sun D, Helmberger D (2008) Lower mantle tomography and phase change mapping. *J Geophys Res Solid Earth* 113:B10305
- Sun DY, Song TRA, Helmberger D (2006) Complexity of D'' in the presence of slab-debris and phase changes. *Geophys Res Lett* 33:L12S07
- Sun D, Helmberger D, Song X, Grand SP (2007) Predicting a global perovskite and post-perovskite phase boundary. In: Hirose K, Brodholt J, Lay T, Yuen D (eds) *Post-perovskite: the last mantle phase transition*, vol 174. American Geophysical Union, Washington D.C., pp 155–170
- Tackley PJ (2011) Living dead slabs in 3-D: the dynamics of compositionally-stratified slabs entering a “slab graveyard” above the core-mantle boundary. *Phys Earth Planet Inter* 188:150–162
- Tackley PJ (2012) Dynamics and evolution of the deep mantle resulting from thermal, chemical, phase and melting effects. *Earth-Sci Rev* 110:1–25
- Takahashi E (1986) Melting of a dry peridotite KLB-1 up to 14 Gpa—implications on the origin of peridotitic upper mantle. *J Geophys Res Solid Earth Planets* 91:9367–9382
- Tateno S, Hirose K, Sata N, Ohishi Y (2005) Phase relations in Mg<sub>3</sub>Al<sub>2</sub>Si<sub>3</sub>O<sub>12</sub> to 180 GPa: effect of Al on post-perovskite phase transition. *Geophys Res Lett* 32:L15306
- Tateno S, Hirose K, Sata N, Ohishi Y (2007) Solubility of FeO in (Mg, Fe)SiO<sub>3</sub> perovskite and the post-perovskite phase transition. *Phys Earth Planet Inter* 160:319–325
- Tateno S, Hirose K, Sata N, Ohishi Y (2009) Determination of post-perovskite phase transition boundary up to 4400 K and implications for thermal structure in D'' layer. *Earth Planet, Sci Lett* 277
- Thomas C, Weber M (1997) P velocity heterogeneities in the lower mantle determined with the German regional seismic network. Improvement of previous models and results of 2D modelling. *Phys Earth Planet Inter* 101:105–117

- Thomas C, Weber M, Wicks C, Scherbaum F (1999) Small scatterers in the lower mantle observed at German broadband arrays. *J Geophys Res Solid Earth* 104:15073–15088
- Thomas C, Kendall J-, Weber M (2002) The lowermost mantle beneath northern Asia? I. Multi-azimuth studies of a  $D''$  heterogeneity. *Geophys J Int* 151:279–295
- Thomas C, Garnero EJ, Lay T (2004a) High-resolution imaging of lowermost mantle structure under the Cocos plate. *J Geophys Res Solid Earth* 109:B08307
- Thomas C, Kendall JM, Lowman J (2004b) Lower-mantle seismic discontinuities and the thermal morphology of subducted slabs. *Earth Planet Sci Lett* 225:105–113
- Thomas C, Wookey J, Simpson M (2007)  $D''$  anisotropy beneath Southeast Asia. *Geophys Res Lett* 34:L04301
- Thomas C, Wookey J, Brodholt J, Fieseler T (2011) Anisotropy as cause for polarity reversals of  $D''$  reflections. *Earth Planet Sci Lett* 307:369–376
- Thorne MS, Lay T, Garnero EJ, Jahnke G, Igel H (2007) Seismic imaging of the laterally varying  $D''$  region beneath the Cocos plate. *Geophys J Int* 170:635–648
- Tsuchiya T (2003) First-principles prediction of the P-V-T equation of state of gold and the 660-km discontinuity in Earth's mantle. *J Geophys Res Solid Earth* 108:2462
- Tsuchiya T, Tsuchiya J (2006) Effect of impurity on the elasticity of perovskite and postperovskite: velocity contrast across the postperovskite transition in (Mg, Fe, Al)(Si, Al) $O_3$ . *Geophys Res Lett* 33:L12S04
- Tsuchiya J, Tsuchiya T (2008) Postperovskite phase equilibria in the MgSiO<sub>3</sub>-Al<sub>2</sub>O<sub>3</sub> system. *Proc Natl Acad Sci USA* 105:19160–19164
- Tsuchiya T, Tsuchiya J, Umemoto K, Wentzcovitch R (2004) Phase transition in MgSiO<sub>3</sub> perovskite in the Earth's lower mantle. *Earth Planet Sci Lett* 224:241–248
- Usui Y, Hiramatsu Y, Furumoto M, Kanao M (2005) Thick and anisotropic  $D''$  layer beneath Antarctic Ocean. *Geophys Res Lett* 32:L13311
- van der Hilst RD, de Hoop MV, Wang P, Shim S-, Ma P, Tenorio L (2007) Seismostratigraphy and thermal structure of Earth's core-mantle boundary region. *Science* 315:1813–1817
- Wallace M, Thomas C (2005) Investigating  $D''$  structure beneath the North Atlantic. *Phys Earth Planet Inter* 151:115–127
- Walte N, Heidelberg F, Miyajima N, Frost D (2007) Texture development and TEM analysis of deformed CaIrO<sub>3</sub>: implications for the  $D''$  layer at the core-mantle boundary. *Geophys Res Lett* 34:L08306
- Walte NP, Heidelberg F, Miyajima N, Frost DJ, Rubie DC, Dobson DP (2009) Transformation textures in post-perovskite: understanding mantle flow in the  $D''$  layer of the Earth. *Geophys Res Lett* 36:L04302
- Wang YB, Guyot F, Yeganehhaeri A, Liebermann RC (1990) Twinning in MgSiO<sub>3</sub> perovskite. *Science* 248:468–471
- Weber M (1993) P-wave and S-wave reflections from anomalies in the lowermost mantle. *Geophys J Int* 115:183–210
- Weber M, Davis JP (1990) Evidence of a laterally variable lower mantle structure from P-waves and S-waves. *Geophys J Int* 102
- Weber M, Kornig M (1990) Lower mantle inhomogeneities inferred from PcP precursors. *Geophys Res Lett* 17:1993–1996
- Weber M, Wicks C (1996) Reflections from a distant subduction zone. *Geophys Res Lett* 23:1453–1456
- Weber M, Davis JP, Thomas C, Krüger F, Scherbaum F, Schlittenhardt J, Körnig M (1996) The structure of the lowermost mantle as determined from using seismic arrays. In: Boschi E, Ekström Göran, Morelli A (eds) *Seismic modelling of the Earth's structure*. Istituto Nazionale di Geophysica, Rome, pp 399–442
- Wentzcovitch RM, Tsuchiya T, Tsuchiya J (2006) MgSiO(3) postperovskite at  $D''$  conditions. *Proc Natl Acad Sci USA* 103:543–546
- Wolf GH, Bukowski ST (1987) Theoretical study of the structural properties and equations of state of MgSiO<sub>3</sub> and CaSiO<sub>3</sub> perovskites: implications for lower mantle composition. In: Manghnani Murli H, Syono Y (eds) *High-pressure research in mineral physics*. American Geophysical Union, Washington, D.C., pp 313–331

- Wookey J, Kendall JM (2007) Seismic anisotropy of post-perovskite and the lowermost mantle. In: Hirose Kei, Brodholt John, Lay Thorne, Yuen David (eds) Post-perovskite: the last mantle phase transition. American Geophysical Union, Washington, D.C., pp 171–189
- Wookey J, Kendall J- (2008) Constraints on lowermost mantle mineralogy and fabric beneath Siberia from seismic anisotropy. *Earth Planet Sci Lett* 275:32–42
- Wookey J, Kendall JM, Rumpker G (2005a) Lowermost mantle anisotropy beneath the north Pacific from differential S-ScS splitting. *Geophys J Int* 161:829–838
- Wookey J, Stackhouse S, Kendall JM, Brodholt J, Price GD (2005b) Efficacy of the post-perovskite phase as an explanation for lowermost-mantle seismic properties. *Nature* 438:1004–1007
- Wyssession ME, Lay T, Revenaugh J, Williams Q, Garnero EJ, Jeanloz R, Kellog LH (1998) The D'' discontinuity and its implications. In: Gurnis M, Wyssession ME, Knittle E, Buffet BA (eds) The core-mantle boundary region, vol 28. American Geophysical Union, Washing D.C., pp 273–298
- Xu W, Lithgow-Bertelloni C, Stixrude L, Ritsema J (2008) The effect of bulk composition and temperature on mantle seismic structure. *Earth Planet Sci Lett* 275:70–79
- Yamazaki D, Yoshino T, Ohfuji H, Ando J, Yoneda A (2006) Origin of seismic anisotropy in the D'' layer inferred from shear deformation experiments on post-perovskite phase. *Earth Planet Sci Lett* 252:372–378
- Young CJ, Lay T (1990) Multiple phase-analysis of the shear velocity structure in the D region beneath Alaska. *J Geophys Res Solid Earth Planets* 95
- Zha C, Bassett W, Shim S (2004) Rhenium, an in situ pressure calibrant for internally heated diamond anvil cells. *Rev Sci Instrum* 75:2409–2418
- Zhang F, Oganov AR (2006) Mechanisms of Al<sup>3+</sup> incorporation in MgSiO<sub>3</sub> post-perovskite at high pressures. *Earth Planet Sci Lett* 248:69–76